

**RADIATION TOLERANCE AND SIGNAL RISE TIME OF THE CMS
PIXEL DETECTOR**

By

Joaquin Emilio Siado Castañeda

A thesis submitted in partial fulfillment of the requirements for the degree of

MASTER OF SCIENCE

in

PHYSICS

UNIVERSITY OF PUERTO RICO
MAYAGÜEZ CAMPUS

July, 2013

Approved by:

Ángel M. López, Ph.D.
President, Graduate Committee

Date

Erick Roura Davila, Ph.D.
Member, Graduate Committee

Date

Juan Eduardo Ramírez Vargas, Ph.D.
Member, Graduate Committee

Date

Carlos Quiñones, Ph.D.
Representative of Graduate Studies

Date

Rafael A. Ramos, Ph.D.
Chairperson of the Department

Date

Abstract of Dissertation Presented to the Graduate School
of the University of Puerto Rico in Partial Fulfillment of the
Requirements for the Degree of Master of Science

**RADIATION TOLERANCE AND SIGNAL RISE TIME OF THE CMS
PIXEL DETECTOR**

By

Joaquin Emilio Siado Castañeda

July 2013

Chair: Ángel M. López
Major Department: Physics

The Compact Muon Solenoid (CMS) is one of the main experiments at the large hadron collider (LHC). This thesis presents the study of two important features of the CMS pixel detector.

The first study shows the performance of the present sensor technology as a function of the irradiation levels comparable to those expected at an upgraded LHC. Thus, it establishes a reference point for the lifetime of the detector. The study also shows changes in the operation voltage of the detector as a function of the irradiation levels. Pixels were irradiated using positive protons of 2.6 MeV and tested using a Sr-90 source.

The second study refers to the timing response of the pixels when a signal passes through them. As the bunch crossing time in the LHC is 25 ns, pixels have to send their data on time to avoid information loss. The study shows the timing response as a function of the irradiation levels as well as the geometric location of the pixels in the array. To measure this time a new technique was developed which resulted in greater precision.

Resumen de Disertación Presentado a Escuela Graduada
de la Universidad de Puerto Rico como requisito parcial de los
Requerimientos para el grado de Maestría en Ciencias

**TOLERANCIA A LA RADIACION Y TIEMPO DE RESPUESTA DEL
DETECTOR DE PÍXELES EN CMS**

Por

Joaquin Emilio Siado Castañeda

Julio 2013

Consejero: Ángel M. López
Departamento: Física

Uno de los experimentos principales en el Gran Colisionador de Hadrones (LHC) es el “Compact Muon Solenoid” (CMS). Esta tesis describe el estudio de dos importantes características del detector de pixeles del CMS.

El primer estudio muestra el desempeño del sensor con la actual tecnología en función de los niveles de irradiación esperados de un LHC actualizado. Por consiguiente, se establece un punto de referencia para el tiempo de vida del detector. Este estudio también muestra los cambios en el voltaje de operación del detector en función del nivel de irradiación. Los pixeles se irradiaron usando protones de energía 2.6 MeV y se estudiaron usando una fuente radioactiva de estroncio 90.

El segundo estudio se refiere al tiempo de respuesta de los pixeles cuando una señal los atraviesa. Ya que el tiempo entre colisiones en el LHC es de 25 ns, los pixeles tienen que enviar su información a tiempo y así evitar la pérdida de ésta. El estudio muestra el tiempo de respuesta de los pixeles como función de los niveles de irradiación, así como de la ubicación geométrica de éstos en la matriz. Para medir este tiempo se implementó una nueva técnica, que da como resultado una medida más precisa.

Copyright © 2013

by

Joaquin Emilio Siado Castañeda

To my parents: Hernan Siado and Nayibis Castañeda, and to my brother Luis Ricardo and my sister Liceth Patricia, for all their unconditional love.

ACKNOWLEDGMENTS

First of all, I would like to thank Dr. Ángel M. López for giving me the opportunity to work in the CMS pixel collaboration. He supervised and guided this work and I truly appreciate his valuable comments and contributions to finish this thesis.

I wish to thank the PSI pixel team for all the knowledge they shared with me in lectures and discussions. I thank Alice Bean and Tilman Rohe for all their questions and help in the data acquisition and analysis process. I appreciate the help provided by Jennifer Sibille and Jose Lazo-Flores in the code implementation and software problems. My gratitude to Frank Meier for organizing the hiking trips where we all had a lot of fun. I would like to thank Anita Van Loon-Govaerts for her guidance through all the political process of being in Switzerland.

Finally, I would like to thank Dr. Juan E. Ramírez and Dr. Erick A. Roura for being part of my graduate committee.

To all my friends for their company in all these years.

TABLE OF CONTENTS

	<u>page</u>
ABSTRACT IN ENGLISH	ii
ABSTRACT IN SPANISH	iii
ACKNOWLEDGMENTS	vi
LIST OF TABLES	ix
LIST OF FIGURES	x
LIST OF ABBREVIATIONS	xii
1 Introduction to the LHC and CMS	1
1.1 The LHC Experiment	1
1.2 The Compact Muon Solenoid	3
1.2.1 CMS Subdetectors	3
1.3 This Study	5
1.4 Overview	5
2 The CMS Pixel Detector	6
2.1 The Module	7
2.2 The Silicon Sensor	8
2.3 Readout Pixel Architecture	9
2.3.1 Token Bit Manager	10
2.3.2 The Double Column Periphery	10
2.3.3 The Analog Readout	10
2.4 Qualification of the Pixel Detector	14
2.4.1 Functionality Test	14
2.4.2 Calibration Tests	15
2.4.3 Performance Tests	16
2.4.4 Important DACs	16
3 Radiation Effects in Silicon Sensor	18
3.1 Energy loss of charged particles in silicon	18
3.1.1 Interaction with Electromagnetic Radiation	19
3.1.2 Electron-Hole Pair Generation	20
3.2 Radiation damage induced in silicon	20
3.2.1 Type inversion	21
3.2.2 Charge trapping	21

4	Risetime Study	23
4.1	Risetime Introduction	23
4.2	Risetime Measurement	23
4.2.1	DAC-DAC Tests	24
4.3	Comparison of the methods	27
5	Experimental design	31
5.1	Test Setup Description	31
5.1.1	Cold Box	31
5.1.2	Sr-90 Source	32
5.2	PSI46 Software	34
5.3	Testing Procedure	34
6	Results of the Charge Collection in Irradiated Sensors	36
6.1	Operation Voltage and Charge Collected	36
6.2	Relative Charge Collection Efficiency	38
6.3	Pixel Detector Performance	39
7	Results of the Risetime Measurements	41
7.1	Comparison with previous results	41
7.2	ROCs without Sensor	41
7.3	ROCs with Sensors	43
7.4	Radiation Effects	44
7.5	Position Dependence	44
8	Temperature Dependence	46
8.1	Introduction	46
8.2	Results	46
9	Conclusion and Future Work	52
9.1	Charge Collection Efficiency	52
9.2	Risetime Study	52
9.3	Future Work	53

LIST OF TABLES

<u>Table</u>		<u>page</u>
7-1	Risetime values for two different methods.	42
7-2	Risetime results for all ROCs with sensors.	44
7-3	Risetime measured as a function of the fluence received by the sensors. . .	45

LIST OF FIGURES

<u>Figure</u>	<u>page</u>
1-1 The CERN accelerator facilities with the locations of the four main experiments: ATLAS, CMS, LHCb and ALICE, as well as the acceleration process.	2
1-2 A cut view of CMS detector showing its different components.	4
2-1 Layout of the CMS pixel detector.	7
2-2 (a) Module's components, from the bottom: The base stripes, the 16 ROCs, the silicon sensor, the HDI, the power cable, the signal cable. b) Photograph of a module.	8
2-3 The pixels sensors.	9
2-4 Schematic view of the readout chain.	12
2-5 Readout process of a readout chip with one pixel hit.	13
2-6 Pulse height as a function of the amplitude of the injected signal. For the lowest V_{cal} values, the pulse height could not be measured because the signal was below the threshold.	15
2-7 S-curve fit (an error function) to determine the noise of a pixel.	17
3-1 Measured energy loss distribution for electrons traversing a silicon sensor.	19
3-2 Depletion voltages and effective doping as a function of the fluence for a typical silicon sensor.	22
4-1 A typical shape of $V_{thrComp}-CalDel$ for a single pixel.	25
4-2 V_{cal} vs $CalDel$	26
4-3 $V_{thrComp}-V_{cal}$ Scan including three different WBCs.	27
4-4 Pulse shape curve as a function of time.	28
4-5 Pulse shape curve as a function of time for a single pixel.	29
5-1 Experimental design for charge collection and risetime measurement.	32
5-2 Arrangement of Main Components.	33
5-3 Distributions of cluster size for a unirradiated ROC.	34
6-1 Charge collected as a function of bias voltage.	37
6-2 Leakage Current dependence with the V_{bias} voltage at different fluences.	38

6-3	Charge collected in irradiated sensors.	39
7-1	Risetime distribution for sensorless ROCs.	42
7-2	Risetime distribution for a single sensor ROC.	43
7-3	Map of the risetime as a function of pixel position within a ROC.	45
8-1	Vana as a fuction of temperature.	47
8-2	CalDel as a function of temperature.	48
8-3	Vtrim DAC as a function of temperature.	48
8-4	Vthreshold DAC vs temperature.	49
8-5	MVP value as a function of temperature.	49
8-6	Risetime as it changes with temperature.	50
8-7	Electronic Noise vs temperature for a single ROC.	50
8-8	Leakage current as a function of temperature for a typical ROC.	51

LIST OF ABBREVIATIONS

LHC	Large Hadron Collider.
CMS	Compact Muon Solenoid.
ROC	Read Out Chip.
DAC	Digital to Analog Converter.
CERN	European Organization for Nuclear Research.
TeV	Tera electron-Volt.
SM	Standard Model.
ATLAS	A Toroidal LHC Aparatus.
ALICE	A Large Ion Collider Experiment.
ECAL	Electromagnetic Calorimeter.
HCAL	Hadronic Calorimeter.
HDI	High Density Interconnect.
TBM	Token Bit Manager.
WBC	Writing Bunch Crossing.
UBL	Ultra Black Level.
PUC	Pixel Unit Cell.
Vcal	Calibration Voltage.
RMS	Root Mean Square.
DC	Digital Current.
MIP	Minimum Ionizing Particle.
PSI	Paul Scherrer Institute.

CHAPTER 1

INTRODUCTION TO THE LHC AND CMS

1.1 The LHC Experiment

The large hadron collider (LHC) shown in Figure (1-1) is the world's most powerful and biggest accelerator in particle physics. It was built at the European Organization for Nuclear Research (CERN) in the French-Swiss border outside Geneva, Switzerland. A circular ring accelerator of 27 Km in circumference, using the existing Large Electron-Positron tunnel facilities, the LHC collides proton with proton at an unprecedented center of mass energy of 8 TeV every 25 ns. In a couple of years the LHC is expected to reach its design center of mass energy of 14 TeV. The LHC has already started its mission of taking particle physics beyond the frontiers known up to now by producing new heavy particles not previously observed.

The LHC was built with the aim of allowing physicists to prove or disprove the predictions of different theories of high energy physics especially those relevant to the standard model (SM) and the possible existence of the large family of new particles predicted by supersymmetric theories. The SM describes the world of elementary particles with great accuracy, but there are still many questions unsolved in this theory: Why does an imbalance matter-antimatter exist? Why do the particles have different mass? Does the Higgs boson exist? Solving all these questions is the main task in the LHC experiment. The last of these questions is almost solved. Last June a new particle was discovered at the LHC. CMS and ATLAS found a particle which match all the characteristics described by the standard model for the Higgs boson the spin of that particle has to be measured to assure that the Higgs boson has been found [1].

In order to achieve this goal, the accelerator's luminosity plays a very important role [2]. For a single beam incident on a fixed target the luminosity is defined as the

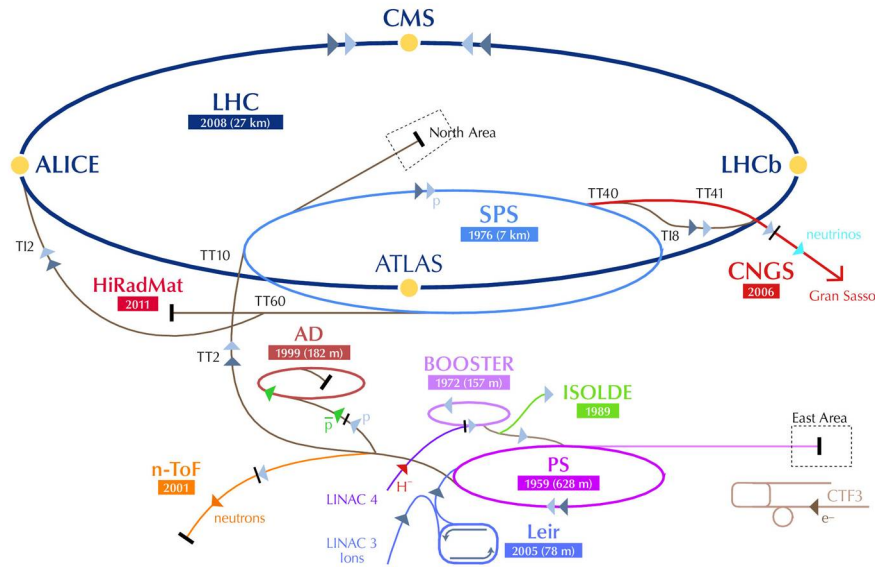


Figure 1–1: The CERN accelerator facilities with the locations of the four main experiments: ATLAS, CMS, LHCb and ALICE, as well as the acceleration process.

number of beam particles incident on a unit area in a unit of time. The number of interactions of a particular process generated in a unit of time is equal to the luminosity multiplied times the cross section for the particular process. The same is true for a collider for which the luminosity can be calculated as [3]:

$$L = fn \frac{N_1 N_2}{A}, \quad (1.1)$$

where f is the revolution frequency of the beams, n is the number of bunches in a beam, N_i is the number of particles in each bunch, and A is the cross-sectional area of the beams which are assumed to overlap perfectly in this formula. The current LHC machine was designed to reach a peak luminosity of $10^{34} \text{ cm}^{-2} \text{ s}^{-1}$. This value will be doubled for upgrade phase I and gradually increased up to $10^{35} \text{ cm}^{-2} \text{ s}^{-1}$ for phase II [4]. Running at this luminosity, the LHC will produce 10^3 charged particles per bunch crossing [2]. With this high flux of particles the detectors in the LHC will need fast and sophisticated detectors to identify all the characteristics of the particles resulting out of the collisions.

Four experiments have been built to complete the goals proposed by the LHC. Two of them, A Toroidal LHC apparatus (ATLAS) and Compact Muon Solenoid (CMS) are large multipurpose experiments [5, 6]. The third experiment is LHCb which is especially dedicated to studying the B mesons [7]. The fourth detector ALICE (A large Ion Collider Experiment), was built to investigate the heavy ion collisions [8]. The main focus of this study is the innermost CMS detector, the pixel detector.

1.2 The Compact Muon Solenoid

The Compact Muon Solenoid is one of the two general purpose detectors in the LHC machine. This means that it can be used to study several physics theories at the TeV energy scale [3]. These theories include: Higgs boson search, looking for extradimensions, and supersymmetry studies. The strong magnetic field generated by the superconducting solenoid allows it to have a compact design (compared with other experiments of its type).

Figure (1–2) shows a layout of the CMS’s subdetectors [9]. They are arranged cylindrically around the beam pipe. Closest to the collision point, a silicon tracking detector determines the trajectories of charged particles as well as the primary and secondary vertices. The tracker is covered by the electromagnetic and hadronic calorimeters which measure the energy of charged and neutral particles. The muon chambers are at the end of the CMS interleaved with iron plates in order to stop the heaviest particles.

1.2.1 CMS Subdetectors

There are many particles with different characteristics: lifetime, charge, mass, etc. In order to identify all this information, the CMS has four subdetectors, each one with different purposes. Starting from collision point they are:

- The Tracker Detector: Composed of silicon, it is segmented into pixels in the innermost region and into strips in the outermost one. Its main function is the reconstruction of primary and secondary vertices. To ensure efficient performance identifying those

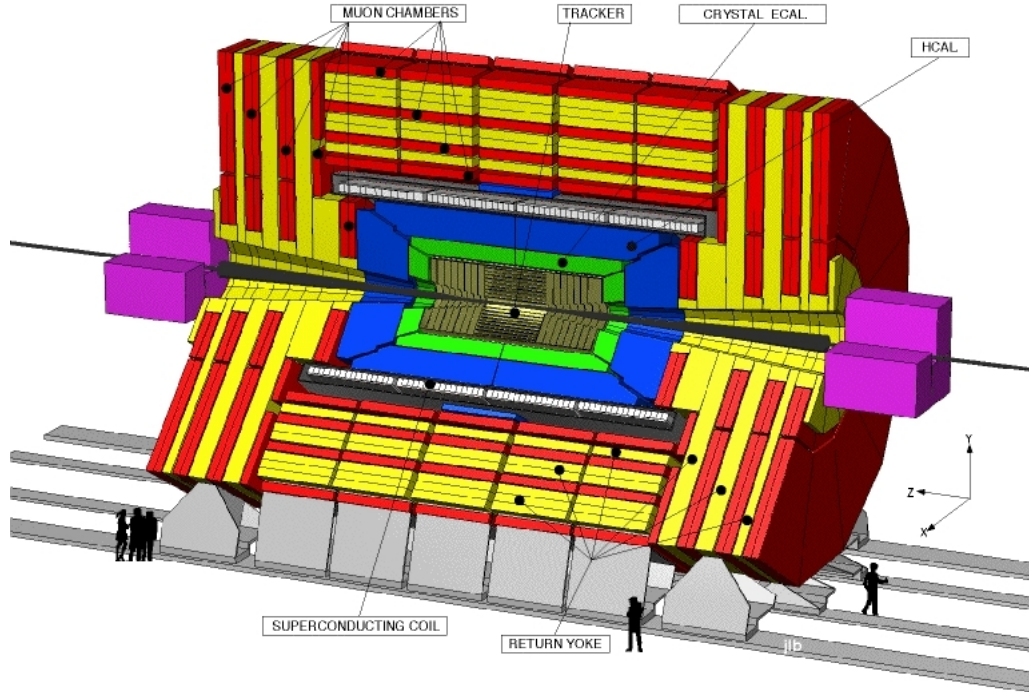


Figure 1-2: A cut view of CMS detector showing its different components.

vertices and correct bunch crossing allocation, a high granularity and a fast response are imperative.

- The Electromagnetic Calorimeter: Surrounding the tracker detector, the Electromagnetic Calorimeter (ECAL) is responsible for identifying and measuring the energy of particles emerging from the collision, especially electrons and photons. Those particles are important, because they are utilized in different channels used to find the Higgs boson.
- The Hadronic Calorimeter: Placed around the ECAL, the hadronic calorimeter (HCAL) is designed to measure hadrons, particles made of quarks and gluons, such as neutrons and protons. It also gives an indirect measure of the uncharged and non-interacting particles like neutrinos.
- The Muon Detector: Because of their large mass (2000 times electron's mass) and low radioactive losses, muons are not stopped in any part of the CMS calorimeters.

Therefore, chambers to detect it are placed at the end of CMS. Muons detection is important because one of the Higgs' final state is identified by four muons.

1.3 This Study

In the phase I of the upgrade, the LHC luminosity will be doubled causing more damage to the components of the pixels. Temperature has to be reduced to allow a better performance of the pixels in such conditions. At present time, the LHC is running at -10°C and will change to -20°C for phase I. This study focuses in analyzing how pixel sensors will respond in a higher radiation and cooler environment. It investigates how the pixel sensor collects charge, moreover how the electronic circuit behaves as the radiation is increased. This study is a continuation of the work presented in [10] with several improvements. These improvements are: the use of a scintillator as a trigger, the humidity control, measure at higher voltage and lower temperatures. In addition, this thesis presents a study of the pixel detection speed using a new method for analysing the data to determine the time it takes to form the pixel signal.

1.4 Overview

The study is presented in the following way: Chapter 2 gives an introduction to the CMS pixel barrel module, its basic components, and the calibration process. The effect of the radiation in the silicon sensors are discussed in Chapter 3. Chapter 4 describes the concept of the preamplifier time and how it is measured. Chapter 5 is dedicated to describe the experimental design used in this work. Results of the studies are presented in Chapters 6, 7, and 8 respectively. Conclusions are reported in Chapter 9.

CHAPTER 2

THE CMS PIXEL DETECTOR

The CMS tracking system consists of two subdetectors: The silicon strip and the silicon pixel detector. The pixel detector is the innermost detector in CMS. It is composed by three cylindrical layers in the barrel region, located at 4.4, 7.2, and 10.2 cm, and two forward pixel disks on each side at a distance of 34.5 cm and 46 cm respectively from the interaction point. Its design was based on the following general principles [11]:

- Precise hit reconstruction: Allowing a precise vertexing.
- Radiation hardness: To reduce the radiation damage during the detector's lifetime.
- Minimal material budget: Minimizing multiple scattering of the particles.
- Reduce noise electronics: This will avoid false hits.

Because of its proximity to the collision region, the pixel detector works in a high radiation environment but, due to its excellent design and construction, it has been a solid performer during the initial CMS run providing two or more hits per track, allowing secondary vertex identification of long-lived objects [3]. The pixel detector geometry is shown in Figure 2-1. Its modular construction allows to insert or remove part of the pixel detector after the installation of the beam pipe. The whole barrel part is 53 cm long and contains a total of 66×10^6 channels [12].

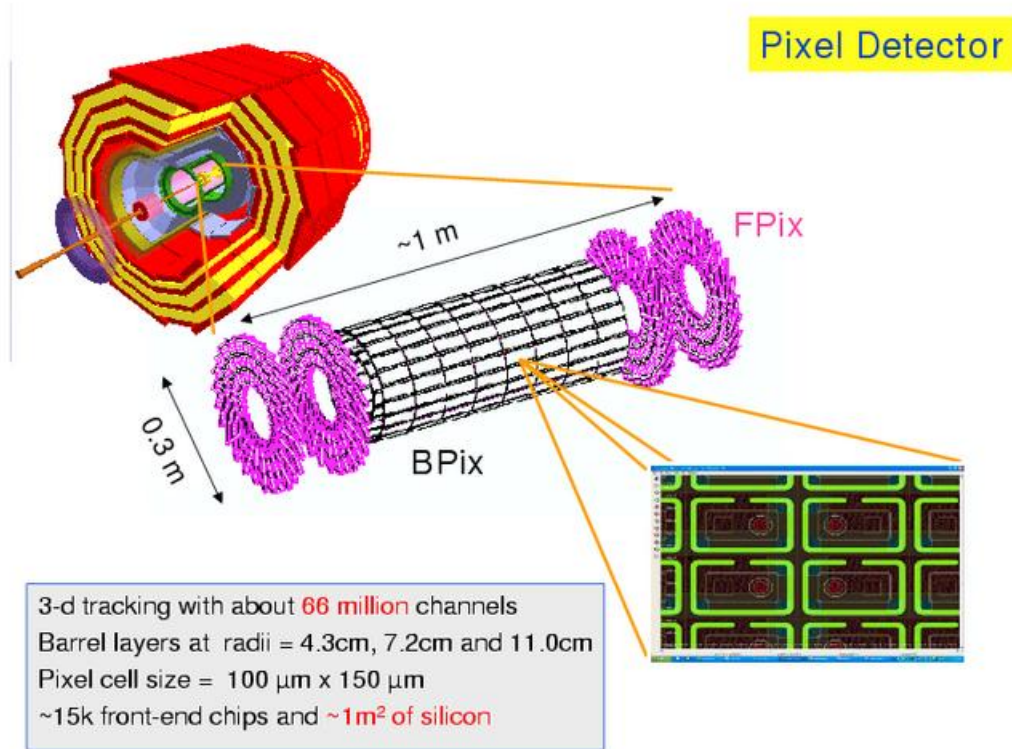


Figure 2–1: Layout of the CMS pixel detector.

2.1 The Module

The barrel region of the pixel detector contains approximately 700 rectangular detector modules of two types: Full modules and half-modules. A full module consists of 16 Read Out Chips (ROCs) (8 for half modules) arranged in a matrix of 2x8 (1x8). Each ROC has 4160 pixels organized in a matrix of 80 rows and 52 columns. The dimensions of the pixel is 100 x 150 μm^2 . Figure 2–2 shows a photograph of a full module and its components.

The connection between the sensor and the ROC is made of indium bumps [13]. These bumps connect each pixel sensor with the pixel unit cell (PUC), the circuit on the ROC that is associated with an individual pixel. On top of the sensor a High Density Interconnect (HDI) serves as an interface to the front end electronics. The connection is established over two cables: The power cable, which supplies the needed voltages and

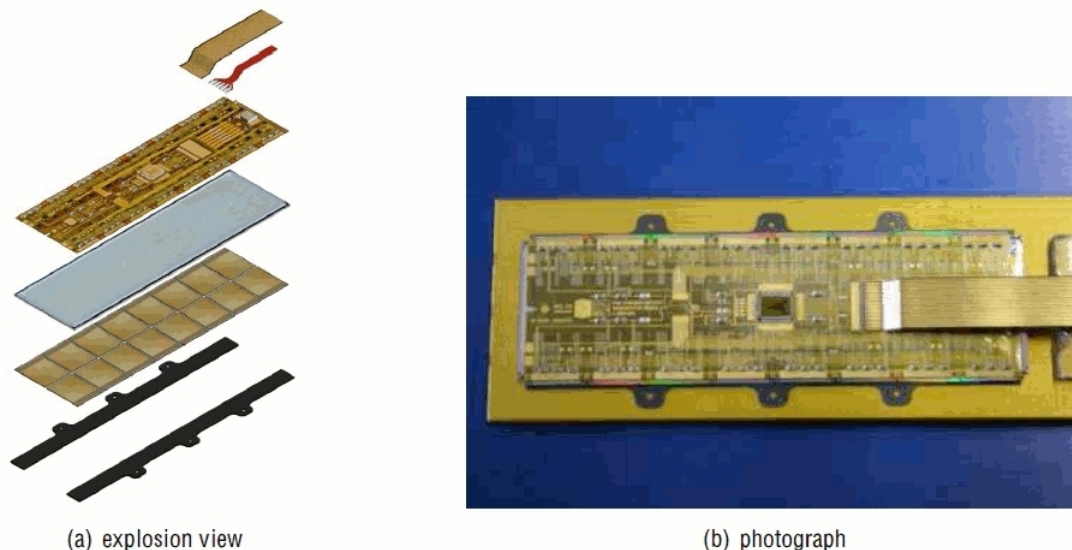


Figure 2–2: (a) Module’s components, from the bottom: The base stripes, the 16 ROCs, the silicon sensor, the HDI, the power cable, the signal cable. b) Photograph of a module.

the signal cable, for the control signals and the analog readout. The chip on the HDI, which organizes the readout of the ROCs, is called Token Bit Manager (TBM). The connection of the HDI to the ROCs was made using wire bonds.

2.2 The Silicon Sensor

The sensor is the basic component of the detector. Here is where the interaction with the radiation takes place. Sensors in CMS are made of silicon. This material was chosen because it is the most studied semiconductor, its electrical properties are well known, and is the commonest element in the earth, which makes it cheaper. The main advantage of silicon is that the energy for producing an electron-hole pair is just 3.6 eV which allows to reach an exceptional energy resolution [14]. By applying an electrical field to the silicon, the carrier depletion region around the diode junction can be expanded to cover the entire sensor area. Electron-hole pairs generated by the passage of a charged particle will not recombine but will move along the electrical field lines and constitute a signal current which is detected by the readout electronics.

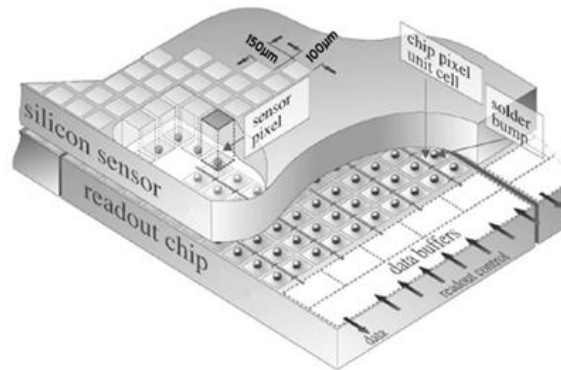


Figure 2–3: The pixels sensors.

In the CMS pixel detector, sensors were built using a n+ implants on a n- type substrate [15]. To achieve a good spatial resolution in both the $r\phi$ and the z-direction¹, an almost squared pixel size was implemented. The sensor thickness is $285\ \mu\text{m}$, which results in an ionization charge of roughly $23\ \text{Ke}^-$ for a minimum ionizing particle traversing the sensor perpendicularly [16]. This value is achieved when the sensor is fully depleted, which occurs at 150V for an unirradiated sensor.

2.3 Readout Pixel Architecture

The pixel detector in the CMS experiment was designed to measure the amount of charge deposited by a particle traversing the sensor. Every pixel is measured every 25 ns which corresponds to the time between bunch crossings at the LHC. This task is done individually for each pixel in its dedicated PUC. As pixels are operated in a zero suppression mode, only those with a signal above a certain threshold are read out. The ROC is divided into two parts: the PUC and the periphery. A complete diagram of the ROC is shown in Figure 2–4. It shows the PUC, the column periphery as well as the control interface block.

¹ r is the radial distance, the azimuthal angle ϕ is measured from the x-axis in the x-y-plane, and z is measure along the beam axes

2.3.1 Token Bit Manager

The token bit manager is placed on the HDI, it has to organize the readout of all ROCs one by one. When a trigger is received, the TBM emits a token to the first ROC. The ROC sends its data to the TBM from the corresponding trigger and passes the token to the next ROC. When all sixteen ROC are read, the whole information is sent from the TBM to the end of the pixel barrel through a kapton cable as analog signal. This information include the pixel address (double column and row) as well as the pulse height and the writing bunch crossing (WBC), a number which identifies the bunch crossing during which the hit was registered.

2.3.2 The Double Column Periphery

The Periphery of the ROC is organized in 26 double columns, containing 160 pixels each. The double column controls the transfer of hit information from the pixels to the storage buffers. The current WBC is stored as an 8-bit value into one of the 16 time stamp buffers. This time stamp is needed later on to associate the hit information with the correct WBC.

2.3.3 The Analog Readout

The readout of the pixels is started and finished by a TBM header and trailer; both consist of eight clock cycles. The TBM header contains three ultra black levels followed by a black level and a level called “last DAC”. An ultra black level (UBL) is simply a mark of the lower bound of the analog signal. A black level defines the zero level of the analog signal. The “last DAC” represents the value of the most recently programmed DAC, or the value of the temperature sensor if no DAC has been programmed since the last cycle. Six clock cycles are added per hit pixel: Two for the double column index, three for the row index and one for the pulse height information. The TBM trailer consists of two UBLs, two black levels, plus four clock cycles with the TBM status

information. Figure 2-5 displays an example of this readout sequence for a module with a hit in one ROC.

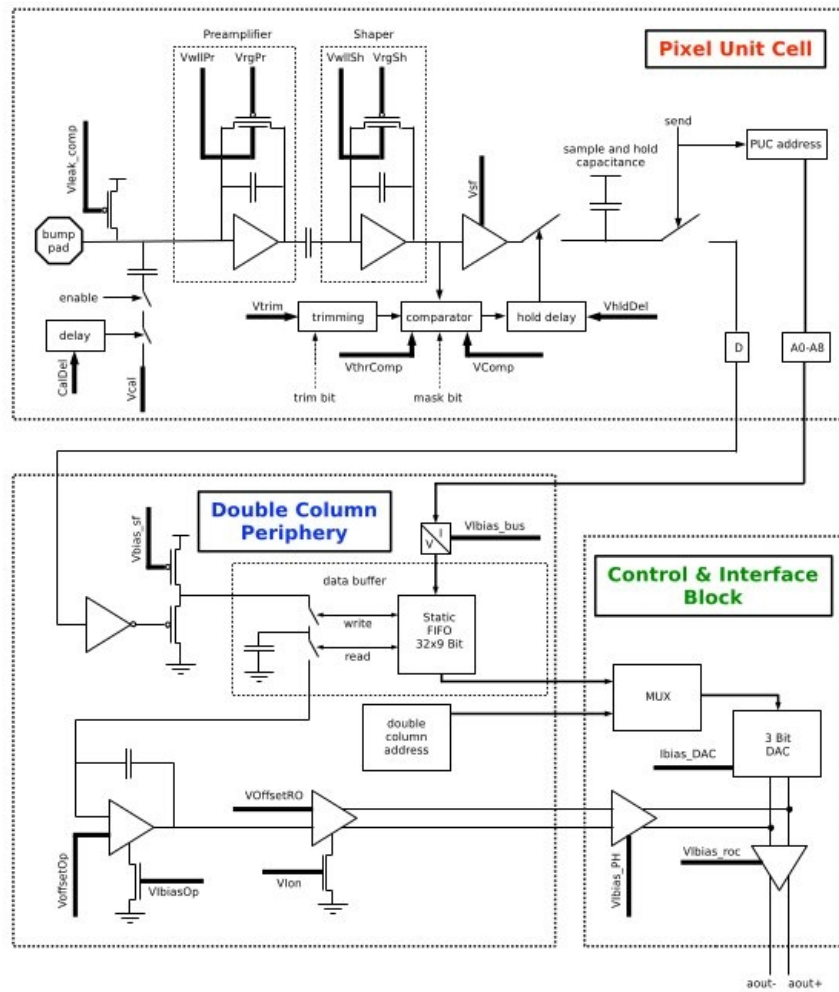


Figure 2-4: Schematic view of the readout chain.

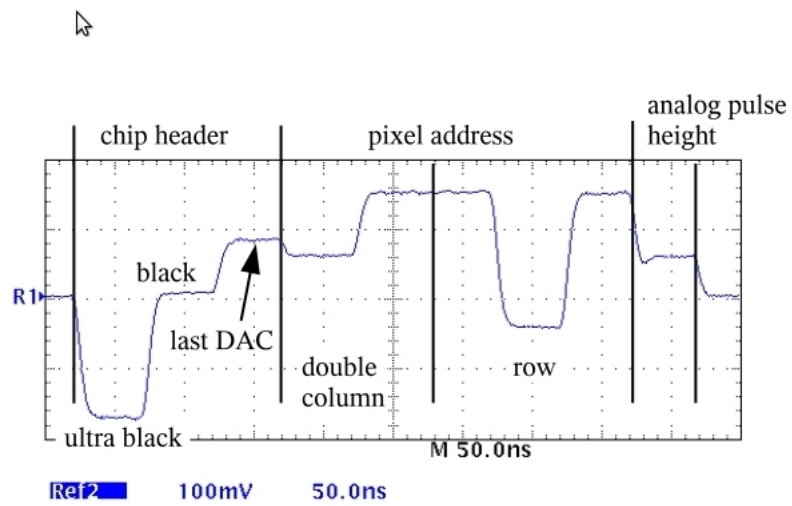


Figure 2-5: Readout process of a readout chip with one pixel hit.

2.4 Qualification of the Pixel Detector

Before it can be placed in CMS, every single module in the pixel detector has to be carefully examined and calibrated. This assures a uniform response over a whole ROC and accurate charge measurements. There are three different kinds of tests that a module has to surpass in order to be considered as a “good” one. These are: Functionality tests, calibration tests and performance tests [17].

2.4.1 Functionality Test

The functionality tests are responsible for the validation of the TBM, the programmability of the pixel readout, and check the bump bond connection.

- **TBM Test:** The TBM is readout in two different modes. In the single mode, the readout of all sixteen ROCs are sent to one analog channel while in a dual mode, the readout is split between two different channels. The third layer of the detector is operated in the single mode, while the first two layers in the dual mode. The TBM test checks that the module can be operated in both modes by checking the number of ROCs of an empty readout.
- **Bump bonding test:** This test checks the quality of the connection between the ROC and the sensor. A calibration signal (V_{cal}) is sent to the ROC surface inducing a charge on the sensor. This simulates a hit in the pixel sensor. This hit is detected if the bump bond is in its optimum condition and undetected if it is missed.
- **Pixel readout test:** This test allows to identify dead pixels, mask defects as well as noisy readout. To check these functionalities in the pixel, a signal of V_{cal} value of 200 is sent to the pixel ten times and read out. If the number of readouts is less than ten or more than ten, the pixel is categorized as dead or noisy respectively. To check the mask bit of a pixel the PUC is disabled; as a result all hits in the pixel are suppressed. Pixels are masked when their electronic noise is too high. Masking those pixels avoids having them overflow a whole double column with false hits.

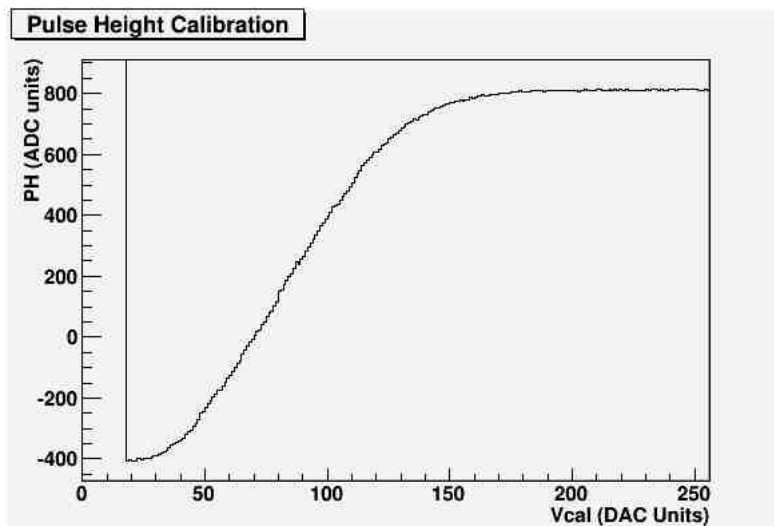


Figure 2–6: Pulse height as a function of the amplitude of the injected signal. For the lowest V_{cal} values, the pulse height could not be measured because the signal was below the threshold.

2.4.2 Calibration Tests

Calibration tests convert an analog to digital converter (ADC) signal into physical units. For example, they convert a measured pulse height into electrons.

- **Pulse Height Calibration:** The ionization charge generated in the sensor by an external excitation is measured as an analog signal (pulse height). It is necessary to convert it to charge (number of electrons). The calibration constants for this conversion are done in two steps. A controlled quantity of charge (V_{cal} calibration signal) is used to determine the pulse height response to each V_{cal} DAC control value. This allows us to convert pulse height to V_{cal} DAC units. Figure 2–6 is a typical curve that is obtained from this test. The pulse height curve is fitted using the hyperbolic tangent function given in equation (2.1).

$$PH(V_{cal}) = p_3 + p_2 \tanh(p_0 x + p_1) \quad (2.1)$$

The relation between V_{cal} units and electrons was obtained in [10] in a separate study using several different X-ray sources. As a result of this study, the conversion factor between V_{cal} and the number of electron-hole pairs generated in the sensor was

found to be $65e^-/\text{Vcal DAC}$. Therefore, when a pulse height resulting from a particle traversing the sensor is measured, it is first converted to Vcal units and then converted to electrons. This magnitude represents the charge deposited in the sensor.

2.4.3 Performance Tests

As it is named, the last kind of test measures the performance of the pixels. For instance, it determines the pixel leakage current and noise.

- Pixel leakage current: Imperfection in the silicon can be detected by measuring the sensor leakage current as a function of the applied bias voltage. If the pixel has problems with scratches or spikes they show up as a breakdown in the sensor at low voltages (around 100 V).
- Noise measurement: The electronic noise of a pixel is determined by measuring the efficiency as a function of the amplitude of the calibration signal. In the absence of electronic noise, this would be a step function, which changes from zero efficiency below the threshold to full efficiency above. The effect of the noise is to smear out the step function in a so-called S-curve. As the noise is assumed to follow a Gaussian distribution, this S-curve is fitted with an error function. The width of the error function is proportional to the noise of the pixel and the threshold is defined as the point where the efficiency response reaches 50%. Figure 2-7 shows the data and the fit for one pixel.

2.4.4 Important DACs

The pixel detector is controlled by 26 Digital to Analog Converters (DACs) and 3 registers, which are adjusted depending on the work conditions. Some DACs control a whole module, others a single ROC and the rest are adjusted for individual pixels. A complete list of all DACs and an explanation of the function for each one can be found in [18]. The most relevant DACs and quantities for this study are: Following are

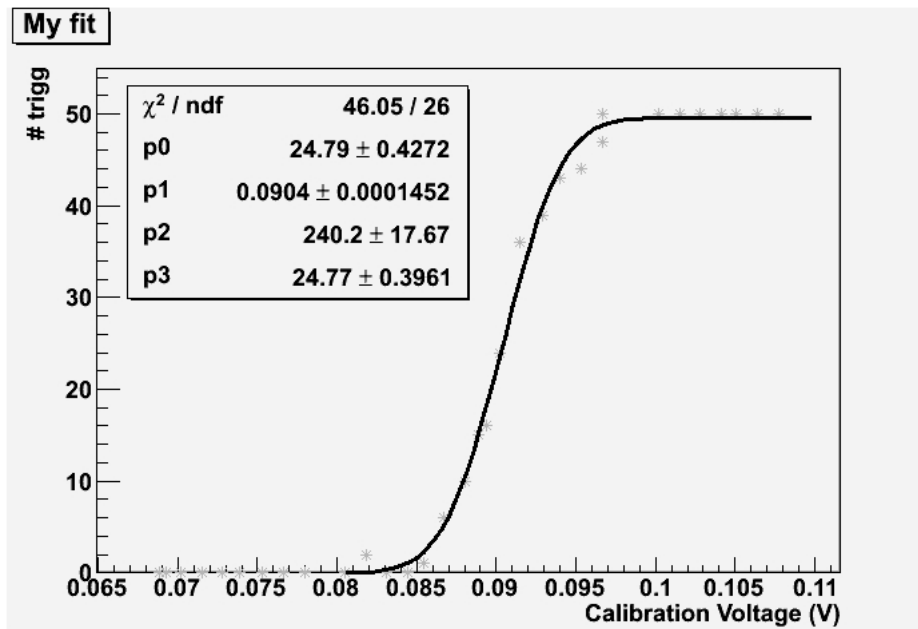


Figure 2-7: S-curve fit (an error function) to determine the noise of a pixel.

the descriptions for the most relevant DACs in this study as well as some important quantities.

- Vsf: The linearity of the pulse height increase as the the Vsf does, but also rises the leakage current. Then, it is set up to the value with linearest pulse height and lowest leakage current. It is set for a whole ROC.
- Vthreshold: This DAC determines the minimum value for a signal to be considered a real event.
- Vtrim: The Vtrim is used to adjust the threshold of the ROC. A global adjustment.
- Vana: Analog operation voltage.
- CalDel: Time delay in injecting the Vcal charge.
- Noise: Is presented in each pixel because of the electronic circuits.
- Leakage Current: Current that flow in the sensor as a consequence of the Vbias voltage even when no particles are passing it.
- Most probable value: When a particle strikes the sensor, ionization charge generation is described by the Landau distribution whose maximum occurs at this value.
- Risetime: Time needed for a signal to rise to 90% of its maximum value.

CHAPTER 3

RADIATION EFFECTS IN SILICON SENSOR

Particles are detected if they transfer energy to the medium they are traversing. One of the ways this transfer can occur is via the process of ionization of the constituent atoms. As the pixel detector is placed in the innermost region of the CMS, it will have a high track density of particles which will eventually cause a considerable damage to the sensors and to the electronics. This damage is manifested in the pixels as: (1) an increase of the leakage current, (2) type inversion, (3) increase of the full depletion voltage, and (4) charge trapping. The following two sections will summarize the main aspects of the interaction between radiation and silicon as well as the damage caused by radiation.

3.1 Energy loss of charged particles in silicon

When a charged particle passes through the silicon, it deposits part of its energy. By measuring this energy it is possible to reconstruct the trajectory of the particle. The energy deposited by a particle is described by the Bethe-Bloch formula, given in the equation (3.1) [19].

$$\left[\frac{dE}{dx} \right] = D_e \left(\frac{Z_1}{\beta_1} \right)^2 n_e \left[\ln \frac{2mc^2 \beta^2 \gamma^2}{I} - \beta^2 - \frac{\delta(\gamma)}{2} \right], \quad (3.1)$$

where $D_e = 4 \pi r_e^2 m c^2 = 5.0989 \times 10^{-25}$, Z is the atomic number, β is the velocity, n_e is the number of electrons per unit of volume, γ is the Lorentz factor and δ is the density effect correction for high particle energies. As the ionization is subject to statistical fluctuations, the value returned by (3.1) is just the average of the so-called Landau distribution, shown in Figure 3–1. Due to the tail, this mean value is larger than the most probable value of the distribution.

β -particles (electrons) are used in the laboratory to test silicon detectors because they produce a uniform charge cloud as long as their velocity remains relativistic. The

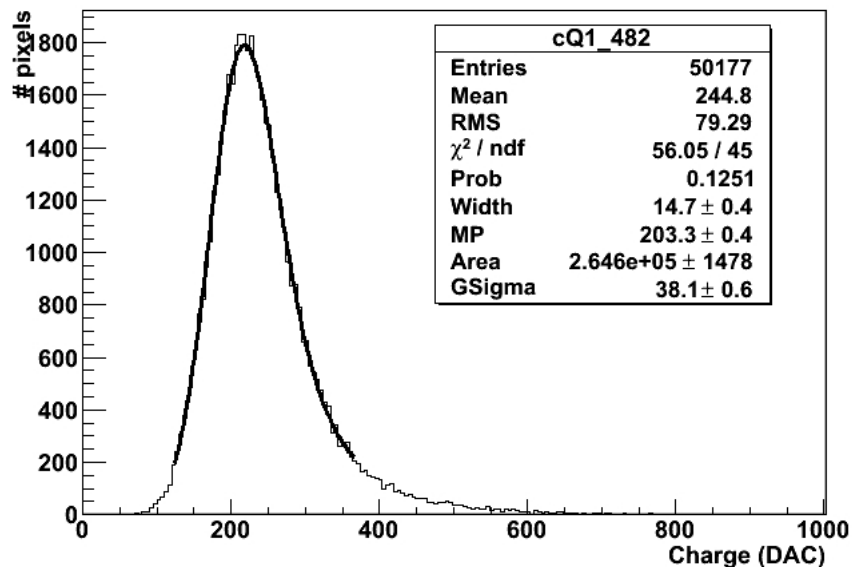


Figure 3–1: Measured energy loss distribution for electrons traversing a silicon sensor.

curve in Figure 3–1 is not exactly a Landau because there is noise in the measurement. The noise follows approximately a Gaussian distribution, so the curve in Figure 3–1 is fitted using a Landau convoluted with a Gaussian function. There are two important parameters in this fit: the most probable value of the Landau, which is a measure of the energy deposited by the particles and the width of the Gaussian which is a measure of the noise.

3.1.1 Interaction with Electromagnetic Radiation

Silicon detectors can interact with electromagnetic radiation (photons) in a wide range of the spectrum. This interaction occurs mainly via three processes: Photoelectric effect, Compton effect and pair production. The intensity of a photon beam going through some material is attenuated according to

$$I(x) = I_0 e^{-\left\{\frac{x}{\mu}\right\}}, \quad (3.2)$$

being I_0 and $I(x)$ the beam intensity before and after traversing a medium of thickness x . μ is known as the attenuation length of the material and depends on the photon energy.

3.1.2 Electron-Hole Pair Generation

The ionization energy deposited by a particle traversing some material is proportional to the number of electron-hole pairs generated. The energy required to produce one electron-hole pair in silicon is 3.6 eV. Equation (3.3) gives the energy E deposited by a particle generating N electron-hole pairs.

$$E = (3.6N) \text{ eV}, \quad (3.3)$$

3.2 Radiation damage induced in silicon

Besides interacting with the electrons in the atoms of a material, some particles also interact with the nuclei. The interaction knocks the nucleus out of its lattice position. This produces crystal imperfections changing the electrical properties of the silicon. Point defects are caused by a single atom displaced out of its original position. But, if the displaced atom gets enough energy, it can cause further defects creating a cluster of defects. Charged particles produce more point defects as they scatter via electromagnetic interaction while neutrons produce more clusters of defects as they only feel the nuclear interaction. The minimum energy necessary to remove a silicon atom from its position is about 25 eV. This minimum energy is produced by interacting electrons of 260 KeV and by protons and neutrons of 190 eV [20].

In order to quantify the damages caused by different types of particles with different energy, a scale of non ionizing energy loss is defined. This quantity includes all energy deposited in the crystal that does not cause ionization. The scale uses neutrons of 1 MeV as reference particles. A beam of arbitrary particles is said to contain n_{eq} neutrons if it produces the same damage as a beam of n_{eq} neutrons with kinetic energy of 1 MeV.

This relation is expressed mathematically as

$$\Phi_{eq} = \kappa\Phi, \quad (3.4)$$

where Φ denotes fluence and κ is called the hardness factor. It depends strongly on the type of incident particle as well as its energy. It can be calculated as shown in [21]. This factor has been obtained experimentally in several works. For instance, the hardness factor for pions of 193 MeV is 1.14 [22]. Hereafter all fluences are given in neutrons equivalent fluence, $\frac{n_{eq}}{cm^2}$.

3.2.1 Type inversion

The spaces left behind when an atom is moved from its original position are called vacancies. As the silicon is irradiated, these spaces act as recombination centers. Here the dopant species changes its function from donor (n-type) to acceptor (p-type). This process is known as type inversion of the material. The change in the depletion voltage and the absolute effective doping are shown in Figure 3–2 [23]. U_{dep} is the bias voltage applied to the sensor. N_{eff} is the difference of all donor-like states and all acceptor-like states. The point at which N_{eff} reaches a minimum is called type inversion.

3.2.2 Charge trapping

Traps are unoccupied sites in the depletion region of the silicon. They are caused due to the lack of a free electron. As a result, the electrons that generate the signal can be trapped by them. If these electrons are trapped for a time greater than the collection time the signal height is reduced. The charge trapping problem can be ignored if the fluence does not exceed $10^{14} \frac{n_{eq}}{cm^2}$. Beyond this point, the charge collected begins to reduce and decreases to around 50% for fluences of $10^{15} \frac{n_{eq}}{cm^2}$.

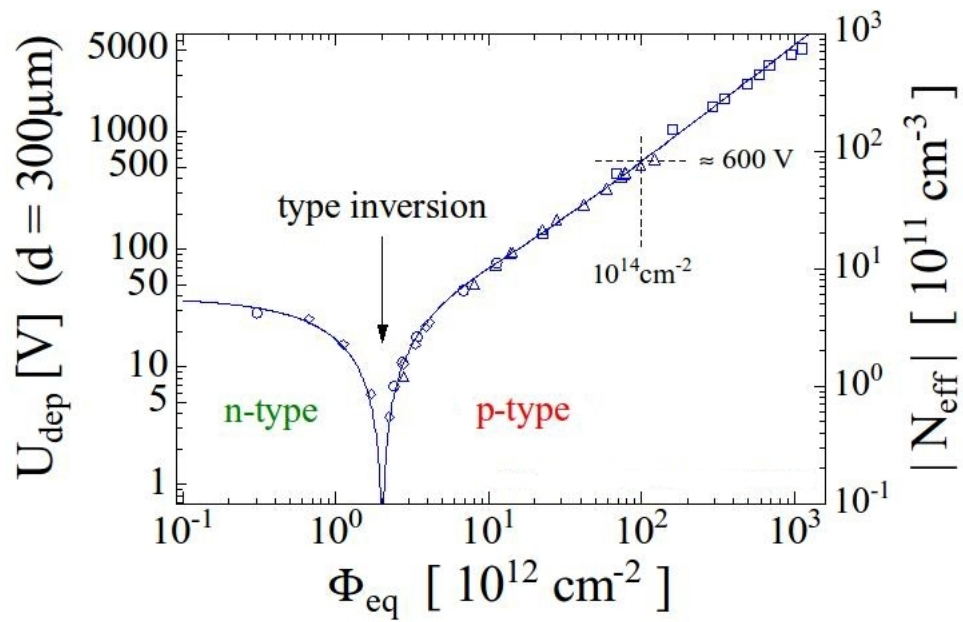


Figure 3–2: Depletion voltages and effective doping as a function of the fluence for a typical silicon sensor.

CHAPTER 4

RISETIME STUDY

4.1 Risetime Introduction

One of the main parts of the pixel readout architecture is the front-end electronics (see Figure 2-4). There the signal is amplified, shaped and sent to the comparator. To ensure a good efficiency in the readout process of the signal, this must be done quickly. Therefore, an important feature of the signal formed by the front-end electronics is its risetime. The risetime is defined as the time taken for the signal to reach 90% of its peak value.

Pixels were designed to have a risetime approximately equal to the bunch crossing time in the LHC machine (25 ns) ???. But the electronics is slightly different for every pixel which implies variations in the risetime values. Also, radiation damage might change this time. One of the objectives of this study is to understand how much is that variation and what is the dependence of the risetime with the radiation doses to the detector. Risetimes which deviate greatly from the standard can render a pixel unusable.

4.2 Risetime Measurement

In order to measure the risetime, a code had already been developed at PSI by other researchers and included in the psi46expert software. This procedure is called PulseShape. Because it is not possible to measure the risetime directly, an alternative method is used. This method consists of three DAC-DAC scans: VthrComp-CalDel, Vcal-CalDel, and VthrComp-Vcal. It is also called the method of threshold analysis via efficiency measurements [24].

4.2.1 DAC-DAC Tests

Each DAC-DAC test works by varying one of the DACs under study while holding the rest of them constant. This process is repeated until all possible combinations of the two DACs are covered. Below is a short explanation for all three tests and what each one does. For each of them, a number of nominally identical calibration signals are sent to the pixel electronic circuit and the number of readouts are recorded. Red color in the following plots means that all sent signals were recorded while the white color means that none of the signals were recorded.

VthrComp-CalDel Test

The VthrComp-CalDel Test is the basis for producing the pulse shape curve. The edges of the "tornado plot" (Figure 4-1) are used to get the pulse shape, i.e. the pulse height versus time dependence. The value of the VthrComp DAC is related to the pulse height since it determines the threshold for the pulse heights that will register. It is important to note that high values of VthrComp correspond to lower thresholds. To obtain the actual pulse height versus time curve we will later need to find the correspondence between VthrComp values and pulse height values. The conversion between CalDel units and nanoseconds it is also needed. For this scan, Vcal is set to a value of 120 which corresponds to injecting an amount of charge equal to the typical amount produced by a pixel when it is hit.

The instant of time at which the pulse height is measured is controlled by the CalDel DAC. For large values of CalDel the calibration pulse will have been delayed too much so that the measurement will have been made too early in the development of the pulse and will not register large enough to surpass the threshold. This gives the white area on the right hand side of the two dimensional plot. As CalDel is reduced, later instants in the pulse development are sampled. For a given threshold, at some instant of time

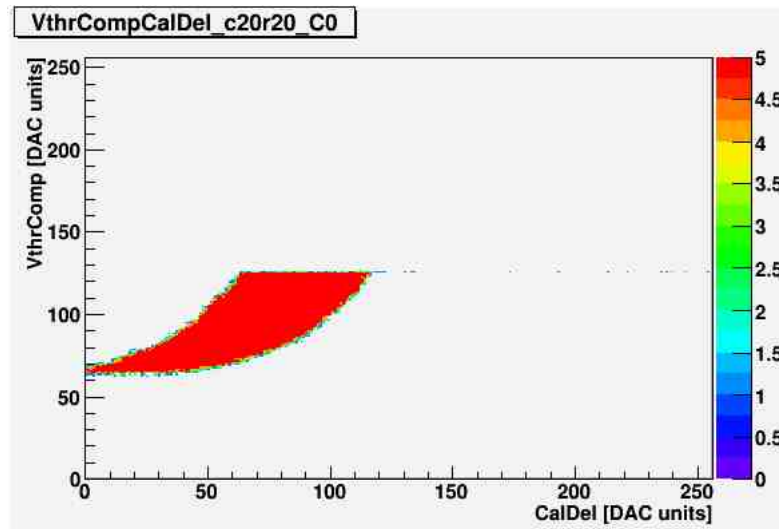


Figure 4–1: A typical shape of VthrComp-CalDel for a single pixel.

the pulse will have reached the threshold and will continue to grow for later times. This manifests itself as the right edge of the tornado plot.

To understand why the left edge of the plot also corresponds to the pulse shape, one has to consider that the pulse height of every pixel is sampled every 25 ns corresponding to the exact time between LHC bunch crossings. Associated with each measurement, there is a whole number which identifies the bunch crossing when the measurement was made. This number is called WBC (writing bunch crossing). As CalDel is reduced further, eventually the pulse is registered in the bunch crossing previous to the one that is plotted and does not register a hit that is counted in this plot. This corresponds to the white area on the left hand side. In other words, only the rising edge of the pulse registers hits and its time development is captured by its appearance in the right edge of the plot and by its movement to the previous bunch crossing in the left edge of the plot.

Vcal-CalDel Test

The purpose of the Vcal-CalDel test is to extract a calibration for the CalDel. The CalDel adjusts the injection time of Vcal in steps in the nanosecond range but we need

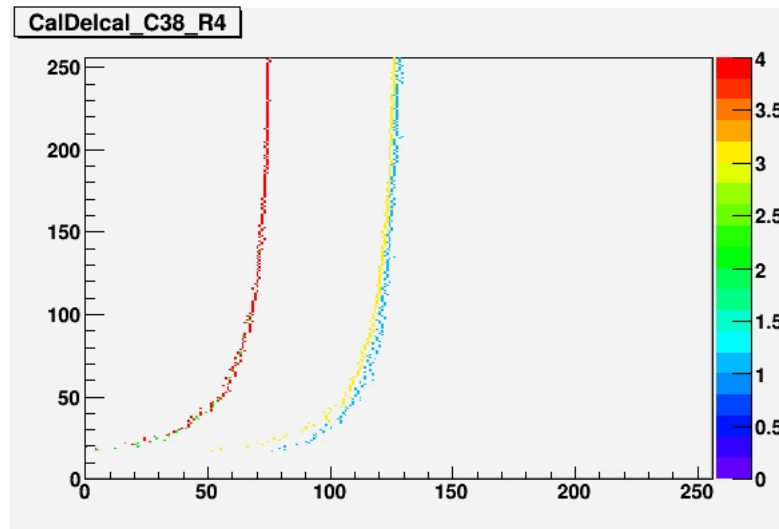


Figure 4-2: Vcal vs CalDel.

a much more precise determination of this conversion factor for each pixel. Figure 4-2 is a typical example of the plots that are produced by this bidimensional scan.

For this scan, the value of VthrComp is set using the tornado plot (Figure 4-1) as the lowest threshold (largest VthrComp) which registers hits. This corresponds to the top edge of the tornado. For most values of Vcal the pulse height will surpass this small threshold almost immediately after its start. Thus the Vcal-CalDel plot has a right edge which is almost vertical for high Vcal values. As in the tornado plot, the left edge corresponds to CalDel values where the pulse has been registered in the previous WBC 25 ns earlier. Thus the width of the plot corresponds to 25 ns and this fact is used to find the conversion factor between CalDel units and nanoseconds. In order to focus attention on the edges, the middle portion of the plot (which would normally be red) has been suppressed.

VthrComp-Vcal Test

VthrComp DAC units must be converted to units which are linearly related to actual pulse height. We will use Vcal units for the latter so we need to determine the

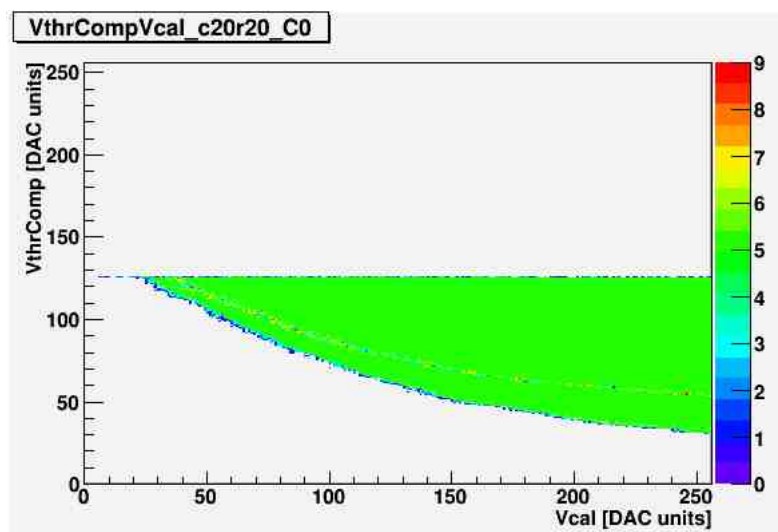


Figure 4-3: VthrComp-Vcal Scan including three different WBCs.

relationship between VthrComp and Vcal units. This is achieved by doing a Vthrcomp-Vcal scan, an example of which is shown in Figure 4-3. Since the time when the Vcal signal surpasses the threshold can change depending on the value of Vcal, all WBCs must be included when doing this plot. Again one of the edges (in this case, the bottom edge) corresponds to the relation between these two units. Since a small value of Vcal is used when doing the VthrComp-CalDel test, we are only interested in establishing the relationship in that Vcal range and it is found that a linear fit to the bottom edge is adequate for our purposes.

4.3 Comparison of the methods

The resulting plot, after DAC-DAC scans are finished and data has the correct units, is shown in Figure 4-4.

This procedure gives the risetime for a single pixel. We want to study pixel to pixel variations so we must repeat this procedure for a statistically significant number of pixels. However, since the procedure takes 35 seconds per pixel, it is not practical to test all 4160 pixels in a ROC. As a compromise, it was decided that only 25% of the pixels would be tested but these were carefully chosen to be evenly distributed in the ROC.

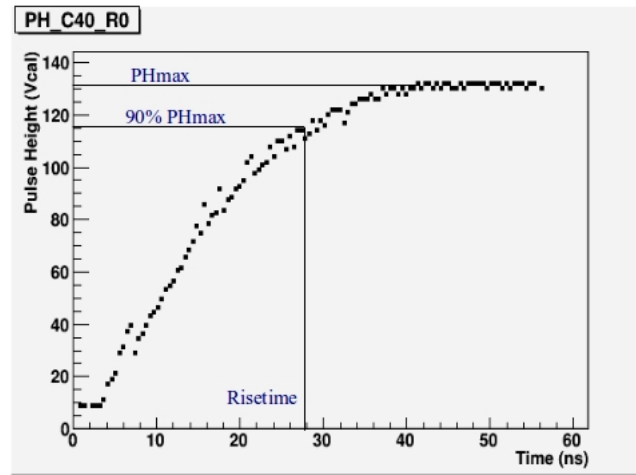


Figure 4–4: Pulse shape curve as a function of time.

In addition, memory saturation software problems reduced the percentage of pixels that could be tested in one session to 6.25% . It took four sessions to complete the test for one ROC. The four output files were then merged and processed offline.

Figure 4–4 also shows how the risetime value was previously calculated. The procedure was as follows: First, the maximum (peak) value of the pulse height was determined (top horizontal line). Then ninety percent of this value was calculated. Finally, the corresponding value in the time axis was taken as the risetime. This technique has some problems. The most troubling is that the data has many fluctuations which introduce uncertainty in the determination of the maximum (the absolute maximum is taken instead of an average of the plateau) and in the determination of the 90% point.

As part of this study a new method to calculate the risetime was developed. The method makes a fit to the curve and extracts the timing parameter from the fitted function. An example of a pulse height curve with its respective fit is shown in Figure 4–5. Due to the fact that there was no theoretical prediction for the pulse shape, several possible fitting functions were studied experimentally. To obtain an adequate fit with a minimum of parameters, it was necessary to fit only over a limited range of times.

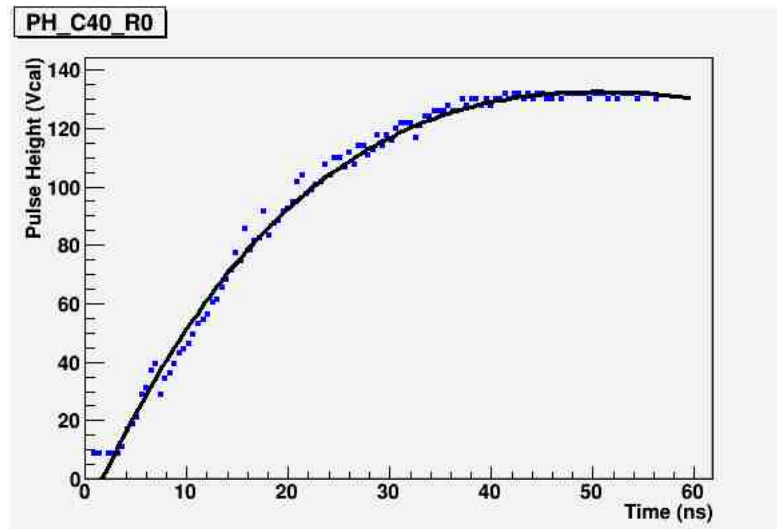


Figure 4-5: Pulse shape curve as a function of time for a single pixel.

This was particularly useful in dealing with the fact that at very early times the data is dominated by noise.

The best fits were obtained with the following fitting function over the range between 15 and 45 ns.

$$PH(t) = p_0 + p_1 t e^{-t/p_2} \quad (4.1)$$

The parameters in the function are: p_0 is the offset, p_1 is the scale and p_2 is the peaking time. The offset adjusts for the noise. The peaking time is the time corresponding to the maximum of this function. Once the fit is done and the three parameters are extracted, the following procedure is followed to calculate the risetime. First, the function (4.1) is evaluated at $t=p_2$ obtaining the maximum of the pulse height (equation (4.2))

$$PH_{max} = p_0 + p_1 p_2 e^{-1} \quad (4.2)$$

Combining (4.1) and (4.2), one obtains (4.3) where t is time at which the pulse height is 90% of the maximum. In other words, t in this equation is the risetime as previously defined.

$$[te^{-t/P_2} - 0.9 * p_2^2 e^{-1}]p_1 + 0.1 * p_0 = 0 \quad (4.3)$$

There is no analytical solution for equation 4.3. A numerical solution is obtained using Newton's method [25]. Since the same definition has been used for risetime, results using this method can be compared directly to the results from the previous method.

CHAPTER 5

EXPERIMENTAL DESIGN

5.1 Test Setup Description

In general the setup used for both studies, charge collection efficiency and risetime measurement, was the same. A photo is shown in Figure (5-1).

It consists of a cold box, a test board, a computer with scientific Linux 5, a high voltage power supply, a Strontium-90 (Sr-90) source [26], a scintillator, an oscilloscope and a trigger system. This setup is similar to the one used in [16, 24], but several changes were made. A scintillator was added to serve as a trigger. This made for much more efficient data collection. In addition the Peltier cooling system was improved so that the temperature could be lowered to -20 C where before it could only reach -10 C.

Circulating water was used to draw heat away from the Peltier elements. The temperature variation was $\pm 0.3^{\circ}\text{C}$. The Sr-90 source was placed 0.8 cm above the sensor. Two delays were applied to synchronize the trigger signal: one between the scintillator and the clock and one applied to the trigger signal. The sensor was placed between the source and the scintillator, as shown in Figure (5-2). The following is a detailed description of the main components.

5.1.1 Cold Box

The cold box is used to control the temperature and humidity of the sensors under study. The -20 Celsius degree temperature was reached using a system of two Peltiers. These devices use the thermoelectric effect. When DC current flows through them heat is transferred from one side to the other. Water flowing through a pipe on the hot side controls its temperature and a lower temperature is achieved on the cold side. Nitrogen gas flowing inside the cold box allowed to keep the relative humidity below 10%. The

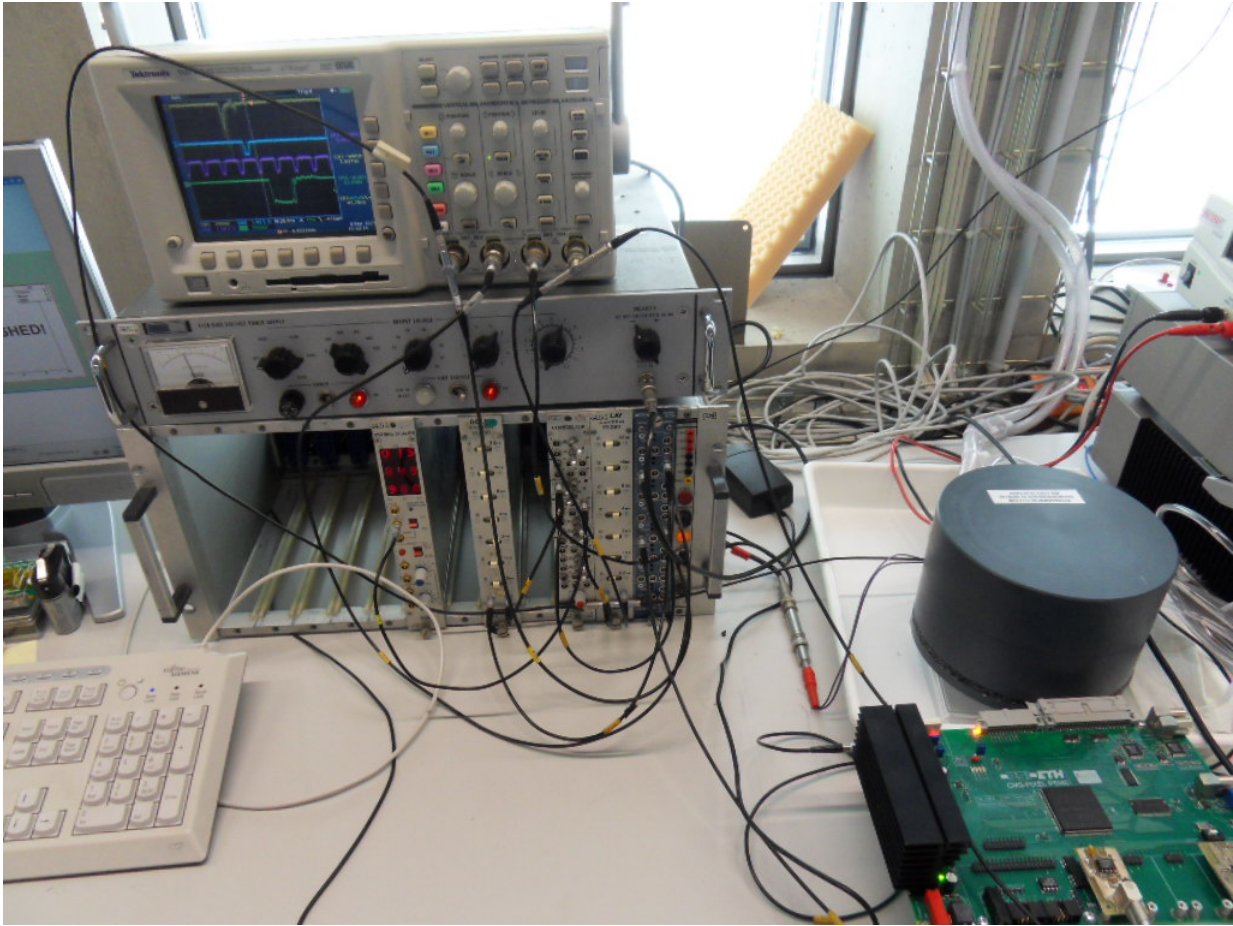


Figure 5-1: Experimental design for charge collection and risetime measurement.

temperature and humidity were measured using a thermocouple and a HIH 4000 sensor respectively.

5.1.2 Sr-90 Source

Iron rings were placed between the sensor and the scintillator to absorb particles that do not go through the sensor perpendicularly. The radiation of the Sr-90 source contains some particles of low energy which cause much higher signal than a minimum ionizing particle (MIP for silicon). If these particles are stopped in the sensor, they can cause electrons to travel in the plane of the sensor ionizing more electrons (secondary ionization), which results in a large number of clusters [16]. Due to the use of the

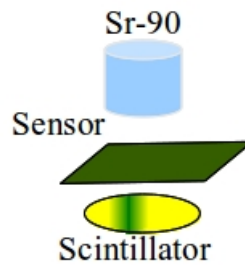


Figure 5–2: Arrangement of Main Components.

scintillator trigger, the number of low energy beta events recorded is greatly reduced. Figure 5–3 shows the distribution of cluster size. Most of the clusters have size 1, which means particles traveling perpendicular to the sensor but, due to the particles passing between pixels or corners there is some fraction with cluster of size two to four. In order to simplify the analysis only hits with cluster size 1 were selected by the offline test software. Due to the distribution of cluster sizes this did not result in a great increase in testing time.

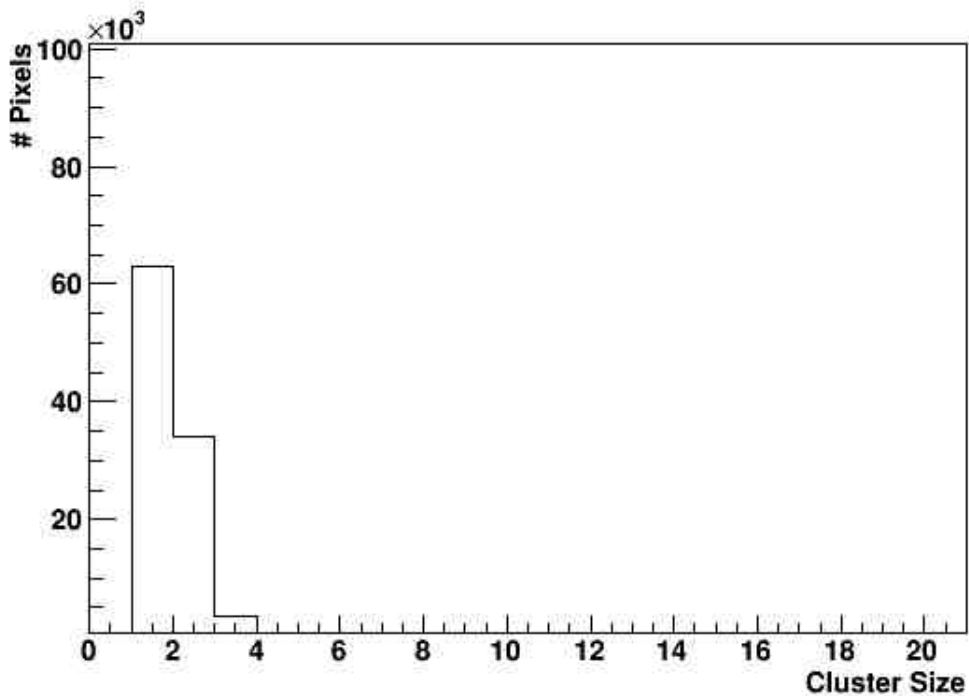


Figure 5–3: Distributions of cluster size for a unirradiated ROC.

5.2 PSI46 Software

In order to test the different operational aspects of the pixels, PSI has developed a series of algorithms dedicated to this purpose and gathered them in a software named `psi46expert`. These tests allow to change the configuration parameters of the ROCs or even individual pixels. Files resulting from the tests are saved in ROOT [27] format permitting to the users analyze the data in more detail.

5.3 Testing Procedure

After pixels are calibrated as described in chapter 2, the data collection can be started. The first test executed is the current vs voltage (I-V) test to check the current's performance as the high voltage is applied. It is the first test because the leakage current flows in the sensor when the bias voltage is applied even when no particles are passing through it [23]. It is also well known that for ROCs that have received a high level of

irradiation a high bias voltage has to be applied [2, 16] and this test can determine what voltage the ROC will be able to withstand. If the pixels do not show any evidence of breakdown, the Sr-90 source is placed just above the sensor. The data acquisition starts at a bias voltage of 20 V and goes on up to 600 V or 1000V depending on the radiation level of the ROC under test. The voltage is increased in 20-volt steps up to 600 V and in 50-volt steps after this value is reached. Each measurement of charge collected takes five minutes. Once this procedure is finished the Sr-90 source is removed and the risetime measurement is started.

CHAPTER 6

RESULTS OF THE CHARGE COLLECTION IN IRRADIATED SENSORS

The results presented here were obtained using ROCs of the same design as the current pixel detector in CMS. We tested unirradiated and irradiated sensors. ROCs with three different doses of radiation 3, 6 and 12 $\times 10^{14} \frac{neq}{cm^2}$ were tested. They were irradiated in Karlsruhe, Germany with 2.6 MeV protons and were stored at -20°C after irradiation to prevent annealing. The data was taken using a Sr-90 source, which emits beta particles with an end-point energy of 2.3 MeV that is approximately equal to the energy of a minimum ionizing particle in silicon.

6.1 Operation Voltage and Charge Collected

Exposing the silicon to radiation causes damage to its crystal structure. As a result of this, an increase in the bias voltage is needed to collect all electrons generated in the sensor and keep the detector working properly. Figure 6–1 shows the dependence of the most probable value of the charge collected on the detector bias voltage for several radiation fluences. For unirradiated sensors the plateau region is easy to appreciate after the full depletion voltage around 90 V. The sensors irradiated up to $6 \times 10^{14} \frac{neq}{cm^2}$, also show a nice plateau above 400 V but at a lower charge collected than the unirradiated one. This means that the amount of charge collected decreases with the fluence. Despite this reduction, the charge collected is still high enough ($\sim 15000e^-$) compared to the threshold ($\sim 4000e^-$). This means that the sensors are still viable at this irradiation level. A similar statement can be made for the sensor that received the highest radiation dose. It reached its plateau at around 800V.

There are several ways that radiation affects the performance of these sensors negatively. One is that it requires the use of higher bias voltages to control losses in efficiency.

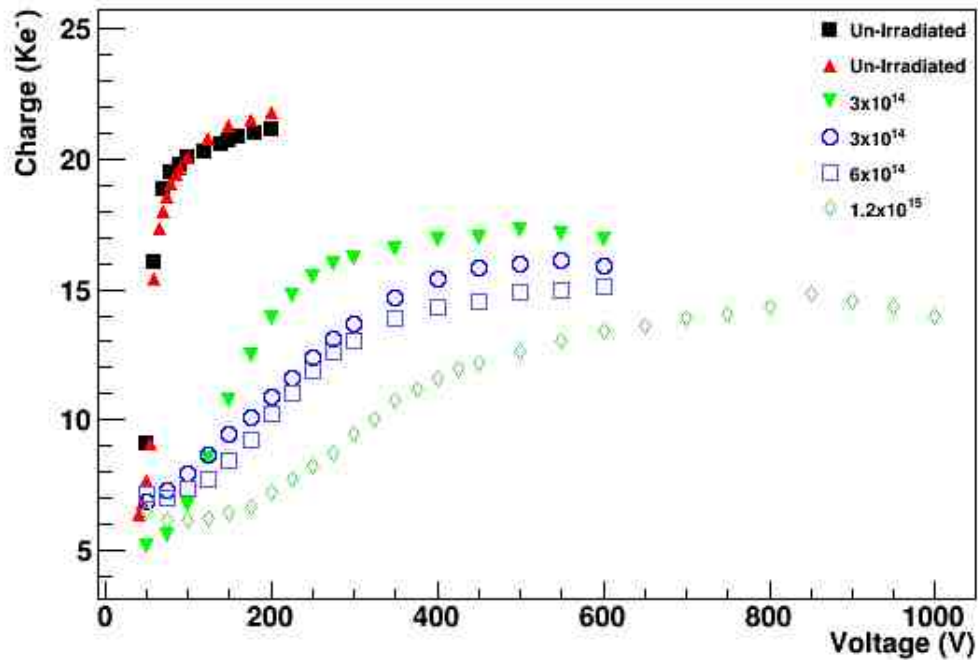


Figure 6-1: Charge collected as a function of bias voltage.

Such voltage increases can cause electrical breakdowns which ruin the sensor completely. Even in the absence of such breakdowns, higher bias voltages will contribute to an increase in the leakage current and an associated increase in the power that the pixel system will consume. Given the limitations on the power that can be supplied to the system, this can become a serious problem.

As it was previously explained, the leakage current might break the pixel if it is too large. In order to avoid this, the leakage current test is the first one done. The bias voltage is increased from zero and the test is stopped if the leakage current reaches a value of $100\mu\text{A}$. Previous studies have shown that breakdown will occur at a leakage current of approximately $124\mu\text{A}$ per ROC.

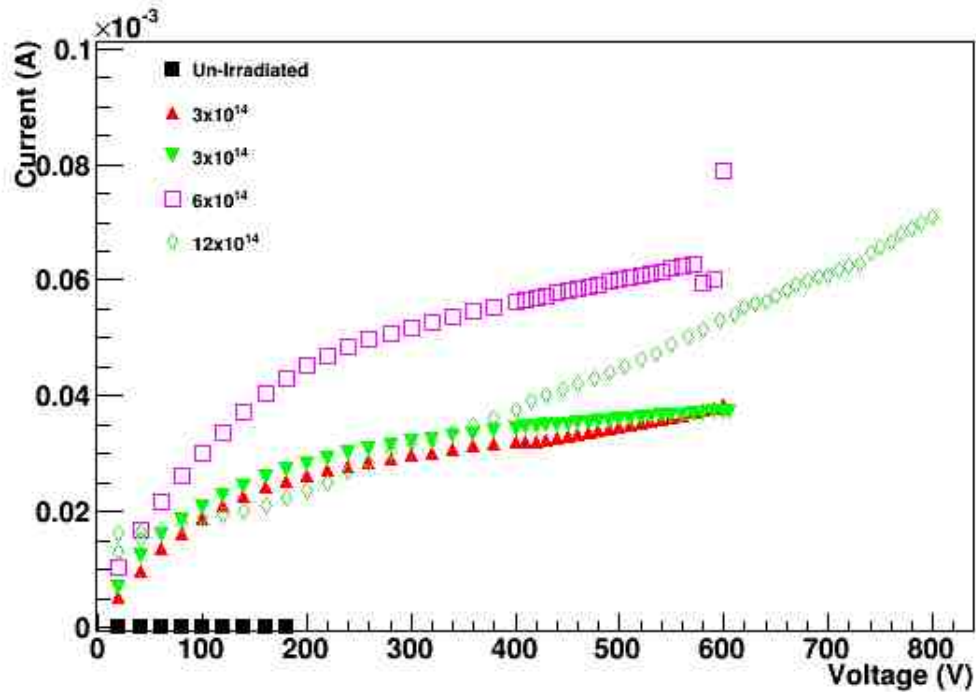


Figure 6–2: Leakage Current dependence with the Vbias voltage at different fluences.

Figure 6–2 shows the leakage current as a function of the radiation in the samples studied. There is no evidence of breakdown in the tested samples. Typically, for an unirradiated ROC the leakage current is a few nA. However, even for the lowest irradiation used here at a bias voltage of only 20 V, the leakage current had increased to the order of a few μA . There is no clear pattern to the rise of leakage current with bias voltage and how it is affected by radiation. Higher radiation doses require higher bias voltages to maintain efficiency resulting in higher leakage currents. These need to be monitored but our results suggest that breakdown will not be a problem even at an irradiation level of $12 \times 10^{14} \frac{n_{eq}}{cm^2}$.

6.2 Relative Charge Collection Efficiency

The absolute efficiency of the detector is defined as the ratio of the number of particles detected to the number of incident particles. Due to the uncertainty on the

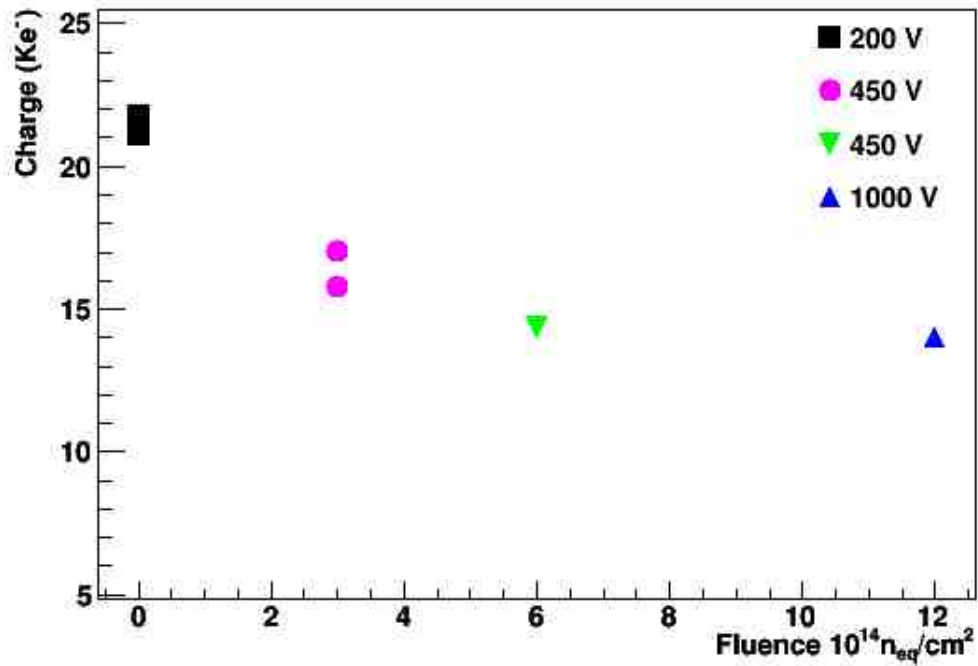


Figure 6–3: Charge collected in irradiated sensors.

number of incident particles introduced by multiple scattering effects, absolute efficiency cannot be measured in our test setup. As an alternative way of characterising sensor performance, we measure the charge collection and compare it to that of an unirradiated sensor. This is shown in Figure 6–3 where we have plotted the charge collected at the plateau bias voltage. (The bias voltages used are indicated in the graph.) This graph allows us to see more clearly the reduction in charge collection with increased radiation. The damage to the silicon by the radiation increases the density of recombination centers where charge carriers can be absorbed and prevented from contributing to the signal.

6.3 Pixel Detector Performance

The luminosity in the LHC increased steadily during its first run and at the end reached $7.7 \times 10^{33} cm^{-2} s^{-1}$ which is nearly 80% of its design luminosity. The integrated luminosity at a center of mass energy of 8 TeV was $\sim 30 fb^{-1}$ which resulted in exposing

the innermost layer of the CMS pixel detector to a fluence of $4.0 \times 10^{13} \frac{n_{eq}}{cm^2}$. In 2018 (phase 1 upgrade) these values will be increased to a luminosity of $2.0 \times 10^{34} cm^{-2} s^{-1}$ and an energy of 14 TeV. During a four year running period the integrated luminosity is expected to be $250 fb^{-1}$ which corresponds to a total fluence of $1.310^{15} \frac{n_{eq}}{cm^2}$ incident on the innermost layer of the pixel detector. This fluence is just above the highest level included in our study. The results found in this work mean that the radiation hardness of the present CMS pixel ROC is such that it can perform adequately in the innermost layer during the LHC Phase 1 upgrade run currently scheduled to occur between 2018 and 2022.

CHAPTER 7

RESULTS OF THE RISETIME MEASUREMENTS

Once the pulse shape test is finished and the data is collected, it is plotted in order to have a better understanding of the pixel response. The pixels that did not respond to the test because they were dead or had bump bonding connection problems were excluded from further analysis. The final results after these cuts are presented below. The numbers that are quoted are the average and the RMS value for the risetime distribution of 1040 pixels in a readout chip, i.e., 25% of the pixels in the ROC.

7.1 Comparison with previous results

The risetime for a few ROCs was measured using both methods. Two sensorless ROCs were measured as well as two ROCs with sensors. None of these ROCs had received radiation. One can compare the results with the old method to the results with the new method by looking at Table 7-1. There is very little difference in the average value for the risetime obtained by either method while there is a significant reduction in the RMS value with the new method. This is attributed to the increased precision offered by the new method while not introducing bias into the measurement. The new method is then a much better way of measuring the risetime of an individual pixel, a parameter of performance which is often used to discriminate between acceptable and not acceptable performance.

7.2 ROCs without Sensor

A total of four ROCs without sensor and unirradiated were tested. Figure 7-1 shows the four distributions and their corresponding average and RMS values. For this kind of ROC the average value of the risetime is 27.1 ± 1.0 ns. The average RMS value of the distributions is 0.8 ns.

Table 7–1: Risetime values for two different methods.

Roc ID	Old Method	New Method
ROC 1	27.1 ± 1.1	27.3 ± 0.8
ROC 2	26.9 ± 1.6	27.1 ± 0.8
8608-3-11	33.1 ± 1.6	32.8 ± 1.2
8606-12-07	29.7 ± 2.5	29.2 ± 2.4

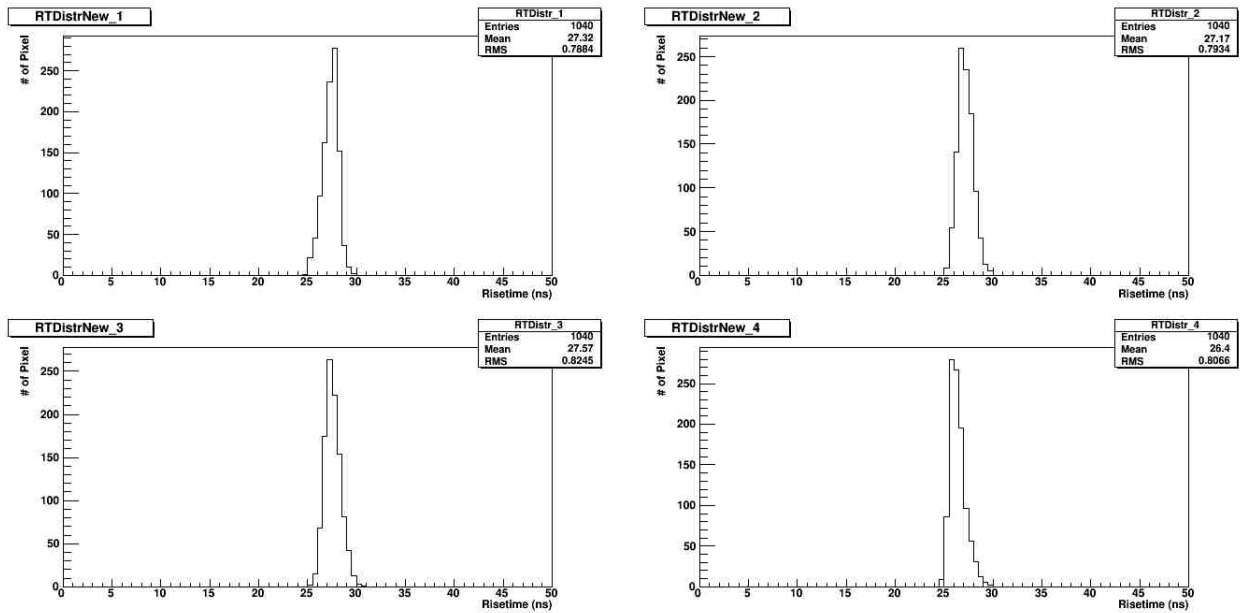


Figure 7–1: Risetime distribution for sensorless ROCs.

7.3 ROCs with Sensors

When the sensor is added to the ROC, it adds an extra capacitance connected in parallel to the one from the readout chip. The effect of this capacitance is to increase the characteristic time of the pixels. Figure 7-2 shows an example of the distribution of risetime values for a single ROC. Only pixels which do not have any anomalous behavior are included and this criterion has been used throughout this analysis.

Table 7-2 shows the results for the rest of the samples analyzed. All these ROCs have an average risetime greater than those ROCs which do not have the sensors on them. This difference is due to the presence of the sensor.

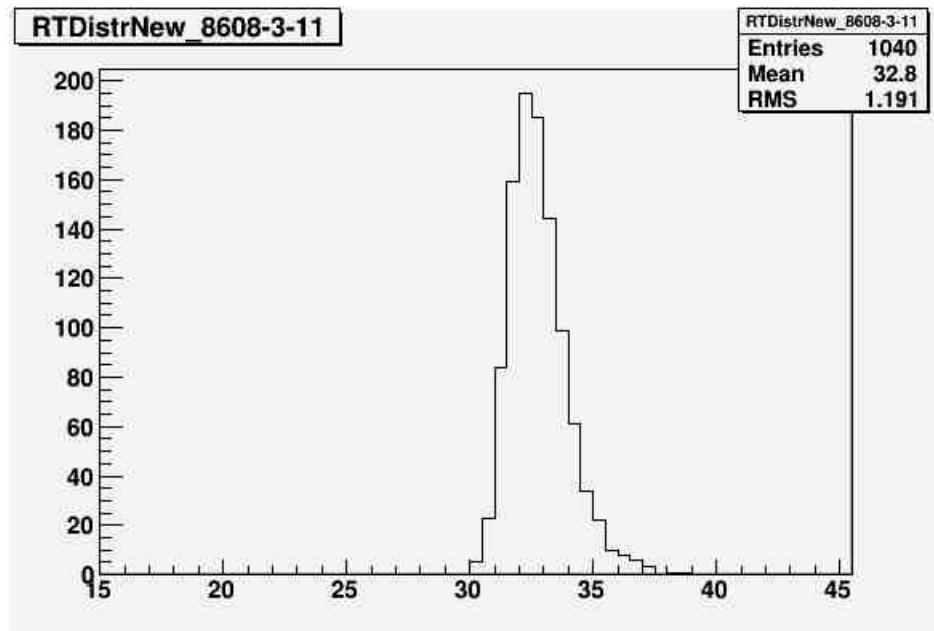


Figure 7-2: Risetime distribution for a single sensor ROC.

Table 7–2: Risetime results for all ROCs with sensors.

Roc ID	Risetime (ns)
8608-3-11	32.8 ± 1.2
8609-11-11	34.0 ± 2.7
8244-17-6	31.0 ± 3.2
8608-13-07	29.2 ± 2.4
8606-12-07	33.1 ± 3.2
8246-05-12	31.0 ± 2.7

7.4 Radiation Effects

Radiation has many different effects on silicon detectors. One of these is to delay the electronics which affects the time response. A group of irradiated ROCs with sensor were tested in order to measure this effect.

Table 7–3 summarizes the results for all measured ROCs. It is observed that the risetime increases when the sensor is exposed to the minimum amount of radiation used in this study. However, the risetime does not increase appreciably with increasing irradiation above this minimum. There seems to be some kind of saturation effect at work. A significant increase in the RMS spread of the risetime among the pixels is also observed.

7.5 Position Dependence

Within the ROC the bias voltage is applied in one of the corners of the pixel array [28]. Figure 7–3 was made to understand if the time response for pixels close to the application voltage point is different from those in the rest of the ROC. No such effect is observed.

Table 7-3: Risetime measured as a function of the fluence received by the sensors.

Roc ID	Fluence ($10^{14} \frac{n_{eq}}{cm^2}$)	Risetime (ns)
8246-15-10	3	38.4 ± 1.6
8246-15-12	3	38.4 ± 2.6
8613-21-05	6	38.5 ± 2.5
8613-08-06	12	38.8 ± 2.8

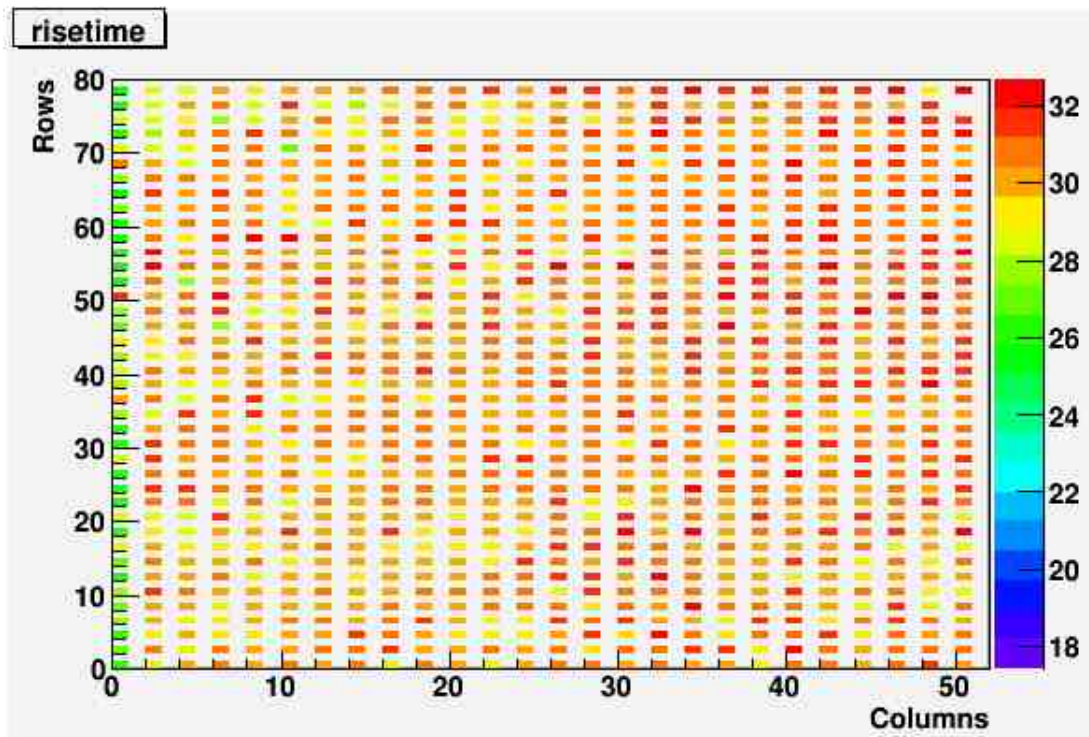


Figure 7-3: Map of the risetime as a function of pixel position within a ROC.

CHAPTER 8

TEMPERATURE DEPENDENCE

8.1 Introduction

In the experimental physics area there are many parameters involved that may change the result of a measurement drastically. One of these parameters is the temperature. Especially in experimental particle physics, temperature control is highly important because most the detectors use electronic components in the readout system. These materials are mostly semiconductors which change their properties with temperature. In consequence, to have an optimum readout of the information in the detector, some DAC parameters in the ROC have to be re-optimized every time that the temperature of the pixel detector is changed. Therefore, is necessary to understand which DACs are dependent on temperature and how is that dependence. A description of the DACs studied in this work can be found in section [2.4.4](#) and the results are presented below.

8.2 Results

Each quantity was measured for eight different temperatures. Starting in 20° , room temperature and finishing in -20° , the operation temperature of the detector.

Figures [8-1](#) to [8-3](#) illustrate changes of the corresponding DACs with temperature. This variation indicate that they should be reoptimized every time that the temperature of the detector is changed. In contrast, Figure [8-4](#) does not show a significant variation of the vthreshold with temperature.

The most probable value, noise, and risetime do not show any dependence with the temperature, as it can be seem in Figures [8-5](#) to [8-7](#). The error bars shown in Figure [8-5](#) are extracted from the width of the Landau distribution. As the risetime and noise are measured for every pixel, the error bars in Figures [8-6](#) and [8-7](#) are the RMS

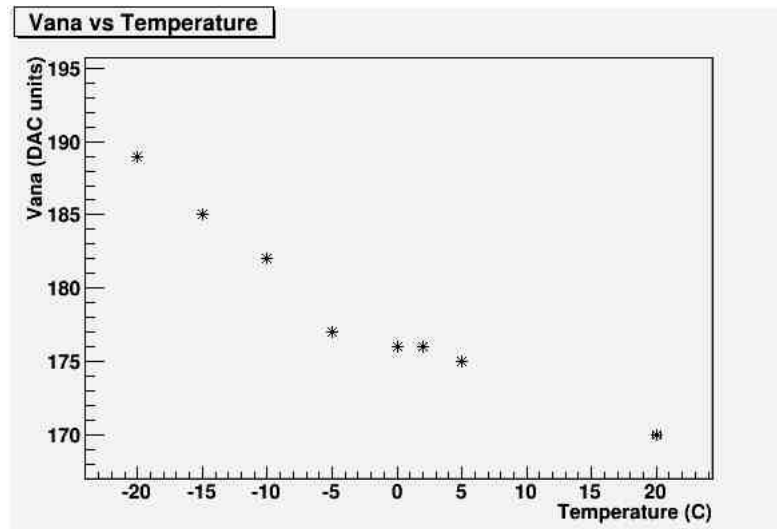


Figure 8-1: Vana as a function of temperature.

of the distribution for an entire ROC. As expected, the leakage current decreases when the temperature is reduced (Figure 8-8).

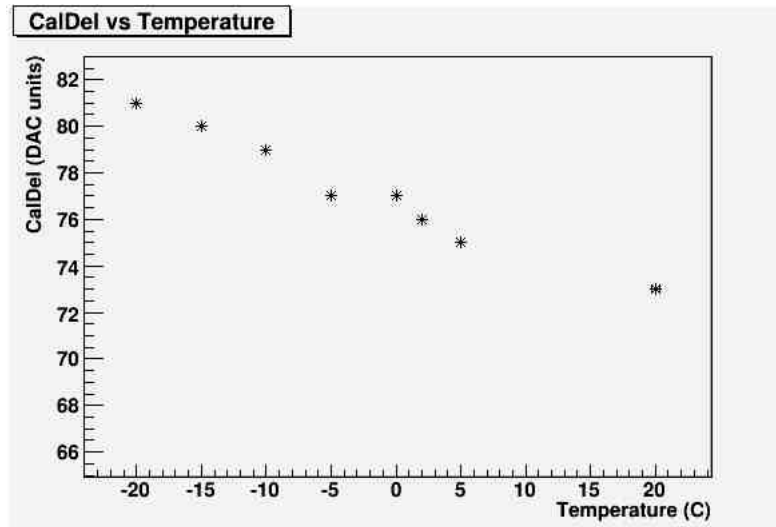


Figure 8-2: CalDel as a function of temperature.

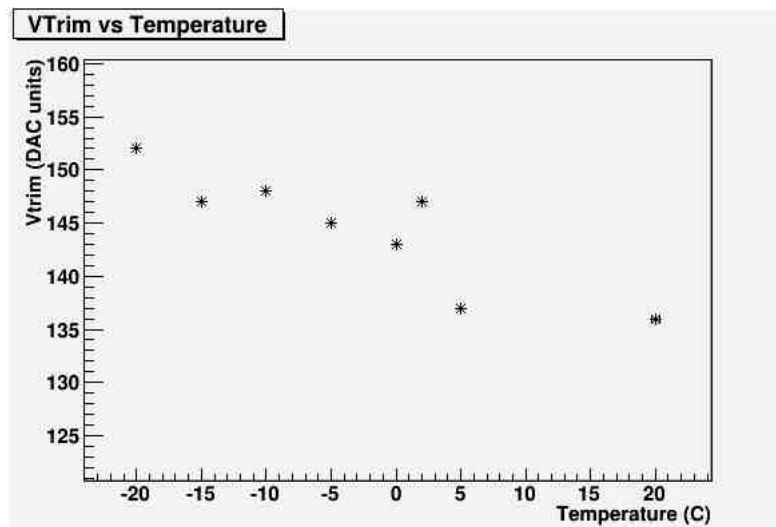


Figure 8-3: Vtrim DAC as a function of temperature.

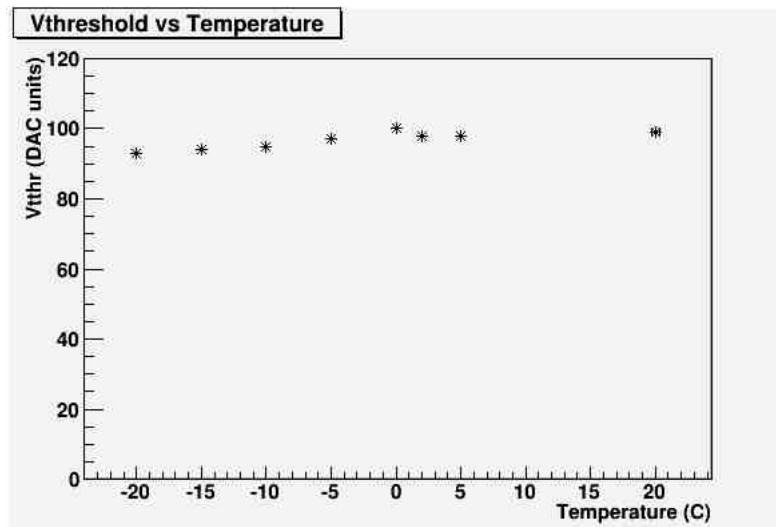


Figure 8-4: Vthreshold DAC vs temperature.

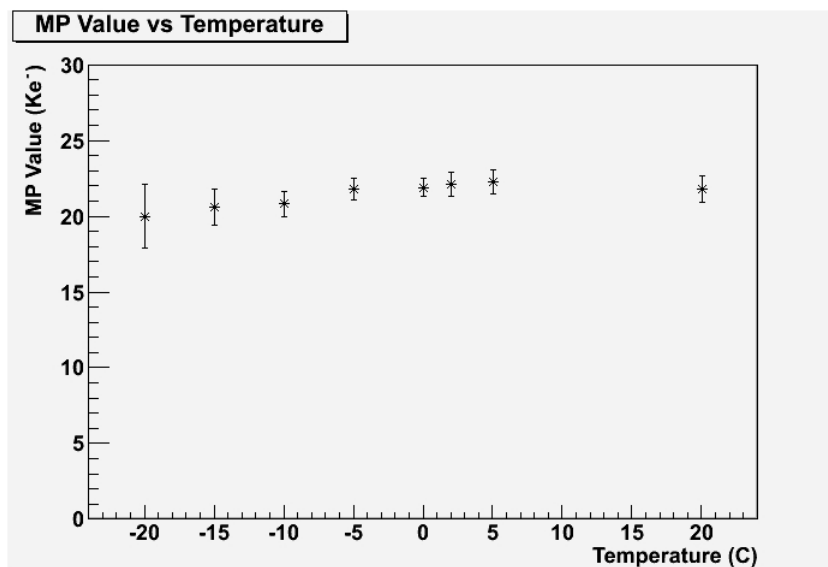


Figure 8-5: MVP value as a function of temperature.

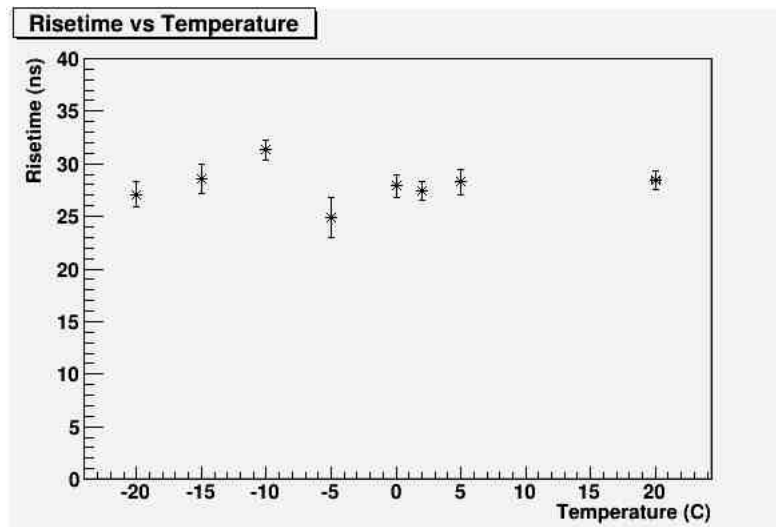


Figure 8-6: Risetime as it changes with temperature.

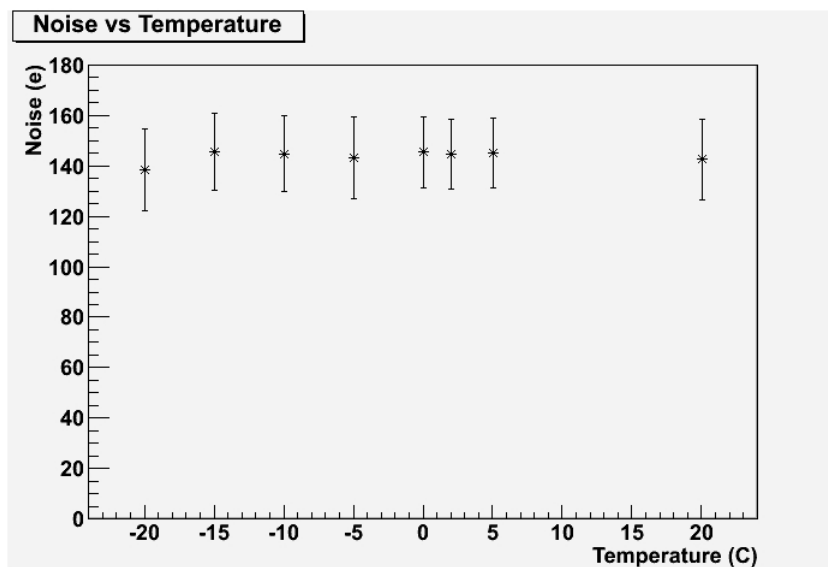


Figure 8-7: Electronic Noise vs temperature for a single ROC.

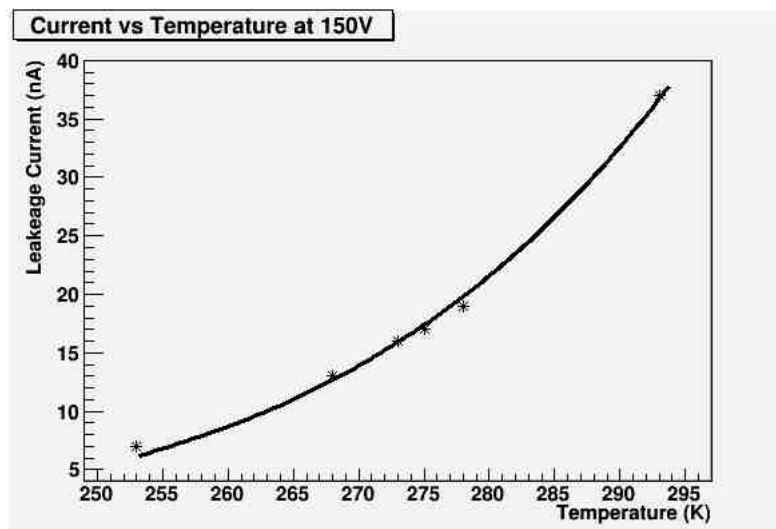


Figure 8-8: Leakage current as a function of temperature for a typical ROC.

CHAPTER 9

CONCLUSION AND FUTURE WORK

In order to know the behavior of the present CMS pixel barrel detector at high radiation doses, sensors have been irradiated to different fluences up to $1.2 \times 10^{15} \frac{neq}{cm^2}$ and tested using a Sr-90 source. Two important aspects concerning the CMS pixel detector behavior under this condition were studied: Chapter 6 described the capacity of the pixels to collect charge and chapter 7 showed the characteristic time of every pixel when it is irradiated. The next two sections summarize the most important results from these two studies.

9.1 Charge Collection Efficiency

The results presented in chapter 6 showed that the current CMS pixel detector is able to work at very high radiation environments with good performance. With samples irradiated at $1.2 \times 10^{15} \frac{neq}{cm^2}$, it is possible to identify a real signal and read it, obtaining a value around $13 Ke^-$. This implies that the current ROC design can be used for the LHC Phase 1 upgrade run which will result in the irradiation of the innermost pixel layer to levels comparable to the highest level used in our study.

9.2 Risettime Study

The signals in the pixel detector must form quickly enough so that the readout is ready to accept another hit that may occur a few bunch crossings later. The performance characteristic that is used to measure the signal shaping speed is called the risetime which may vary from ROC to ROC and from pixel to pixel within a ROC. Comparing Tables 7-2 and 7-3 one can see the increment in the time response of the sensors when they are exposed to high doses of radiation. For unirradiated sensors the average value is approximately 32 ns and this increases up to 39 ns for ROCs that have received a high level of radiation while both are larger than the values for the ROCs with no sensor

on them. Table 7-3 also shows that there is not a large difference depending on the irradiation received by pixels. This result suggests that there is some type of saturation after irradiation.

A major contribution of this work was the development of a new method for extracting the risetime from the pulse height vs. time data. Risetimes determined with the new method were more precise on a pixel to pixel to basis. However, this study found no significant difference for the average risetime for a ROC compared to the results obtained with the previous method.

Another contribution of this study was the understanding of which DACs have a dependence with the temperature. Results in chapter 8 had shown that Vana, Vtrim, and CalDel should be re-optimized if the temperature of the detector is changed.

9.3 Future Work

After finishing this work it is capable of recognizing the limitations and the possible solutions that could be apply. One of the recommendations is to improve the system that supplies the nitrogen to the cold box. It is shared with another test station and when a test is stopped or started at the other station, the pressure of the nitrogen changes and the temperature in the cold box is also changed. Measurement of the risetime for 25% of the ROC (1040 pixels) in the current software takes ten to eleven hours. It is recommended to improve the code in order to reduce the testing time. Finally, two studies are suggested for the future:

- Increase the number of irradiated ROCs tested to have more statistics.
- Test an irradiated ROC without sensor to achieve a better understanding of the saturation of the risetime as a function of irradiation.

REFERENCES

- [1] *CMS collaboration, combined results of searches for the standard model Higgs boson in pp collisions at $\sqrt{s} = 7$ TeV. CERN-PH-EP/2012-023*
- [2] *CMS Collaboration. The CMS Experiment at the CERN LHC. Volume 3, 2008.*
- [3] *C. Hörmann. Design and performance of the silicon pixel detector modules for the CMS experiment. Dissertation, Universität Zürich, 2006*
- [4] *R. Horisberger. Status of pixel upgrade phase I. Presentation from Tracker general meeting, CMS week, CERN 9 april 2013*
- [5] *The Atlas collaboration, CMS Tracker, Technical Design Report LHCC 98-6, CERN, Geneva Switzerland, 1998*
- [6] *The CMS collaboration, CMS Tracker, Technical Design Report LHCC 98-6, CERN, Geneva Switzerland, 1998*
- [7] *LHCb Collaboration, S. Amato et al., LHCb technical proposal, CERN-LHCC-98-04*
- [8] *ALICE: Technical proposal for a large ion collider experiment at the CERN LHC, CERN-LHCC-95-71.*
- [9] *CMS Collaboration. The CMS experiment at the CERN LHC. Journal of Instrumentation, 3 S08004:2677, 2008.*
- [10] *J. Acosta. Study of the Vcal calibration within pixels and study of the macroscopic radiation effects on sensors of the CMS pixel detector, MS thesis. Univ of Puerto Rico, 2010*
- [11] *CMS detector design. <http://cms.web.cern.ch/news/cms-detector-design>.*
- [12] *Milan Bicozza U. Overview of the cms pixel detector. CMS/CR, 2008.*
- [13] *C. Broennimann et al., Development of an indium bump bond process for silicon pixel detectors at PSI, Nucl. Instrum. Meth. A 565, 2006.*
- [14] *C. Kittel. Introduction to solid state physics. John Wiley Sons, Inc, eighth edition, 2005*

- [15] Y. Allkofer et al., *Design and performance of the silicon sensors for the CMS barrel pixel barrel detector*. *Nucl. Instrum. Meth. A* 584, 2008, 25.
- [16] T. Rohe, et al., *Signal height in silicon pixel detectors irradiated with pions and protons*, *Nucl. Instrum. Meth. A* 612, 2010
- [17] R. Horisbergerb, A. Starodumov, W. Erdmannb. *Qualification procedures of the cms pixel barrel modules*. *Nucl. Instrum. Meth. A* 565(1):6772, 2006.
- [18] *PSI Pixel Chip - External Specification, 2005*.
- [19] R Fernow. *Introduction to experimental particle physics*. Cambridge University Press, first edition, 1989.
- [20] Gerhard Lutz. *Semiconductor Radiation Detectors*. Springer, second edition, 2007
- [21] *The ROSE Collaboration: Notes on the fluence normalization based on the NIEL scaling hypothesis*. Technical Note ROSE/TN/2000-02, CERN, Geneva, Switzerland, 2000. <http://rd48.web.cern.ch/rd48/>
- [22] M. Moll et all. *Relation between microscopic defects and macroscopic changes in silicon detector properties after hadron irradiation*, *Nucl. Instrum. B* 186, 2002
- [23] Leonardo Rossi, et al. *Pixel detectors From Fundamentals to Applications*. Springer-Verlag Berlin Heidelberg, 2006
- [24] T. Rohe et al., *Radiation Hardness of the CMS pixel barrel detector* , *Nucl. Instrum. Meth. A* 617, 2010, 534
- [25] Kendall E. Atkinson. *An Introduction to Numerical Analysis*. John Wiley & Sons, Inc, second edition, 1989
- [26] Glenn F. Knoll. *Radiation detection and measurement*. John Wiley & Sons, Inc, fourth edition, 2010
- [27] *ROOT: an object oriented data analysis framework*. <http://root.cern.ch/drupal/content/users-guide>

- [28] *A. Dorokhov, Performance of radiation hard pixel sensors for the CMS experiment, Ph.D. thesis, ETH Zurich, Switzerland, 2005*